



The effect of the number of SO_3^- groups on the adsorption of anionic dyes by the synthesized hydroxyapatite/Mg–Al LDH nanocomposite

Maliheh Heravi¹ · Varsha Srivastava² · Ali Ahmadpour^{1,3} · Vahid Zeynali¹ · Mika Sillanpää^{4,5,6,7,8}

Received: 3 September 2023 / Accepted: 21 January 2024

© The Author(s), under exclusive licence to Springer-Verlag GmbH Germany, part of Springer Nature 2024

Abstract

In this study, a new nanocomposite of hydroxyapatite (HA)/Mg–Al layered double hydroxide (LDH) was successfully formed via a facile co-precipitation method and applied to adsorb three anionic dyes of alizarin red S (ARS), Congo red (CR), and reactive red 120 (RR120) differing in the number of SO_3^- groups from aqueous solution. Based on a combination of characterization analysis and adsorption experiments, HA/Mg–Al LDH nanocomposite showed better adsorption performance than HA and Mg–Al LDH. Using XRD and TEM analyses, the crystallinity and the presence of nanoparticles were confirmed. According to the SEM investigation, the Mg–Al LDH layers in the nanocomposite structure were delaminated, while HA nanorods were formed at the surface of Mg–Al LDH nanoparticles. The higher BET surface area of the novel HA/Mg–Al LDH nanocomposite compared to HA and Mg–Al LDH provided its superior adsorption performance. Considering an effective amount of adsorbent dosage, pH 5 was selected as the optimum pH for each of the three dye solutions. According to the results from the study of contact time and initial concentration, the pseudo-second-order kinetic ($R^2 = 0.9987, 0.9951, \text{ and } 0.9922$) and Langmuir isotherm ($R^2 = 0.9873, 0.9956, \text{ and } 0.9727$) best fitted the data for ARS, CR, and RR120, respectively. Anionic dyes with different numbers of SO_3^- groups demonstrated distinct adsorption mechanisms for HA and Mg–Al LDH nanoparticles, indicating that the adsorption capacity is influenced by the number of SO_3^- groups, with HA/Mg–Al LDH nanocomposite offering superior performance toward dyes with higher numbers of SO_3^- groups. Furthermore, ΔH° less than 40 kJ/mol, positive ΔS° , and negative ΔG° accompanied by the mechanism clarifying show physical spontaneous adsorption without an external source of energy and increase the randomness of the process during the adsorption, respectively. Finally, the regeneration study demonstrated that the nanocomposite could be utilized for multiple adsorption–desorption cycles, proposing the HA/Mg–Al LDH as an economically and environmentally friendly adsorbent in the adsorption of anionic dyes in water treatment processes.

Keywords Adsorption · Anionic dyes · Hydroxyapatite · Layered double hydroxide · Nanocomposite

Responsible Editor: Angeles Blanco

✉ Ali Ahmadpour
ahmadpour@um.ac.ir

¹ Department of Chemical Engineering, Faculty of Engineering, Ferdowsi University of Mashhad, Mashhad, Iran

² Department Research Unit of Sustainable Chemistry, Faculty of Technology, University of Oulu, 90014 Oulu, Finland

³ Industrial Catalysts/Adsorbents and Environment (ICAE) Lab, Oil and Gas Research Institute, Ferdowsi University of Mashhad, Mashhad, Iran

⁴ Department of Biological and Chemical Engineering, Aarhus University, Nørrebrogade 44, 8000 Aarhus C, Denmark

⁵ Department of Chemical Engineering, School of Mining, Metallurgy and Chemical Engineering, University of Johannesburg, P.O. Box 17011, Doornfontein 2028, South Africa

⁶ Functional Materials Group, Gulf University for Science and Technology, Mubarak Al-Abdullah 32093, Kuwait

⁷ Department of Civil Engineering, University Centre for Research & Development, Chandigarh University, Gharuan, Mohali, Punjab, India

⁸ School of Technology, Woxsen University, Hyderabad, Telangana, India

Introduction

The fast rise of industrialization and urbanization over the last few decades has increased the demand for freshwater resources. These developments harmed the ecosystem by releasing various forms of pollutants. Textile industry produces wastewater with high levels of chemical oxygen demand (COD), turbidity, and a varied pH range (Dotto et al. 2019). A significant portion of the textile industrial toxic sludge containing dyes is disposed of into the environment, resulting in a disturbance to the natural balance (Daphedar et al. 2022). Due to the carcinogenic and mutagenic nature of the dyes discharged, these high amounts of dyes are considered a direct threat not only to the human body but also to other soil and aquatic organisms (Mudhoo et al. 2021; Islam et al. 2023). Azo dyes are abundantly available in dye-containing wastewater and can be transformed into aromatic amines with genotoxic and carcinogenic detrimental properties (Hameed and Ismail 2020; Fried et al. 2022). Therefore, developing efficient methods to remove azo dyes from aquatic dye solutions is a major challenge of modern wastewater treatment (Ayati et al. 2014).

Techniques such as aerobic and anaerobic biological technology, membrane separation, coagulation, catalytic degradation, and adsorption have been implemented to remove azo dyes from wastewater (Ayati et al. 2014). Among the above-mentioned methods, the adsorption process has been widely implemented due to its simplicity, efficiency, and low cost (Pai et al. 2020). Organic/inorganic adsorbents and their composites have been extensively used in azo dye removal. Hydroxyapatite (HA) and layered double hydroxides (LDH) are two of the materials that have shown great potential in azo dye removal. HA is an inorganic material that is used in bone tissue engineering due to its unique features such as osteoconductive, biocompatibility, non-immunogenicity, and non-toxicity (Pai et al. 2020; Saharan et al. 2023). It has also been used as a biocompatible adsorbent for the removal of various materials such as dyes, heavy metals, and pharmaceuticals (Ghanavati Nasab et al. 2018; Sadeghizadeh et al. 2019; Marincas et al. 2021). LDHs are two-dimensional adsorbents that consist of layers of bivalent (M^{2+} : Mg^{2+} , Zn^{2+} , Ni^{2+} , Fe^{2+} , Cu^{2+} , etc.) and trivalent (M^{3+} : Al^{3+} , Mn^{3+} , Fe^{3+} , Cr^{3+} , etc.) cations, together with interlayer anions (A^{n-} : CO_3^{2-} , NO_3^- , Cl^- , etc.). LDHs are generally represented as $[M^{2+}_{1-x}M^{3+}_x(OH)_2]^{x+}(A^{n-})_{x/n} \cdot mH_2O$, where x is $M^{3+}/(M^{2+} + M^{3+})$, normally varying between 0.17 and 0.5 (Omran et al. 2022). Di- and trivalent cations are in octahedral positions and possess excessive positive charge (Omran et al. 2022). Advantages such as low cost, low toxicity, reusability, facile synthesis methods, and high

stability have rendered this material a candidate for a wide range of applications such as fuel cells, catalysis, adsorption, and drug delivery (Iftekhhar et al. 2018a, b; Srivastava et al. 2018).

Both HA and Mg–Al LDH have been proven to be efficient anionic dye adsorbents, and their composites with other materials have been introduced to enhance their adsorption capacities (Jiang et al. 2019; Mallakpour and Hatami 2019; Piri et al. 2019; Li et al. 2023). Therefore, it was estimated that the HA/Mg–Al LDH nanocomposite may show a higher adsorption capacity toward anionic dyes. Anionic dyes possess negative charges on their surface that can be adsorbed by positively charged surfaces. In addition, both HA and Mg–Al LDH are porous materials that can provide micro- and mesopores with high specific surface areas for adsorption. Considering the values of adsorption capacities of anionic dyes for these two adsorbents, several parameters such as the number of functional groups, molecule size, and molecular weight of dye may play a role in the adsorption efficiency and capacity of the adsorbents. Because higher molecular sizes and weights lead to higher numbers of SO_3^- groups in anionic dyes, further investigation is needed to identify the mechanisms governing the adsorption of anionic dyes with different numbers of SO_3^- groups. As HA/Mg–Al LDH nanocomposite provides two types of nanoparticles that can adsorb anionic dyes with different mechanisms, using this nanocomposite can demonstrate the mechanisms more clearly.

Therefore, the first objective of the current work was to experimentally synthesize and characterize HA/Mg–Al LDH nanocomposite and investigate its capacity for the removal of three anionic dyes and obtaining the optimum condition to achieve the highest adsorption capacity. The second objective of the present study was to investigate the effect of the number of SO_3^- groups in the anionic dyes on the adsorption capacity of the nanoparticles and the nanocomposite. To the best of our knowledge, such a systematic investigation for the effect of the number of SO_3^- groups in anionic dyes on the adsorption efficiency of HA/Mg–Al LDH nanocomposite has not been explored in the literature. To achieve this goal, three anionic azo dyes with different molecular sizes, which are widely used in the textile industry, were selected for the investigation of the adsorption ability of HA, Mg–Al LDH, and HA/Mg–Al LDH nanocomposite toward them.

Materials and methods

Materials

Orthophosphoric acid (H_3PO_4 , 85%), calcium hydroxide [$Ca(OH)_2$], aqueous ammonia solution (NH_3 , 25%), sodium hydroxide (NaOH, 97%), hydrochloric acid (HCl),

aluminum nitrate nonahydrate ($\text{Al}(\text{NO}_3)_3 \cdot 9\text{H}_2\text{O}$), magnesium nitrate hexahydrate, ($\text{Mg}(\text{NO}_3)_2 \cdot 6\text{H}_2\text{O}$), sodium carbonate (Na_2CO_3), methanol, alizarin red S (ARS), Congo red (CR), and reactive red 120 (RR120) were purchased from Sigma-Aldrich. Deionized water was used for all experiments. The main physicochemical features of the pollutants of ARS, CR, and RR120 are presented in Table 1.

Adsorbent synthesis

HA synthesis

Hydroxyapatite nanoparticles were synthesized via co-precipitation (Shakir et al. 2018). Briefly, calcium hydroxide reacts with orthophosphoric acid, resulting in the precipitation of HA nanoparticles in the form of a white powder. Typically, 0.9 M H_3PO_4 and 1.5 M $\text{Ca}(\text{OH})_2$ solutions were first prepared separately to ensure the stoichiometric Ca/P ratio of 1.67, and then, the acid solution was added dropwise to the calcium hydroxide solution while stirring vigorously and maintaining pH 11 with 25% ammonia solution. The suspension was stirred for 24 h, aged for 48 h at room temperature, and then the white precipitate was filtered, washed until neutralization, dried at 110 °C for 24 h, and ground. HA synthesis steps are graphically summarized in Figure S1.

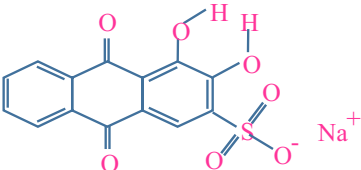
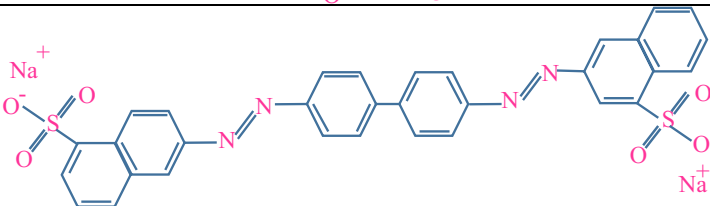
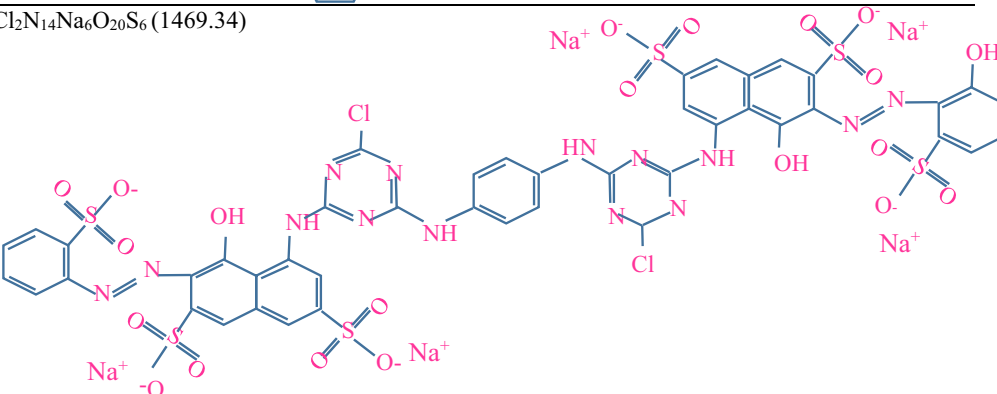
Mg–Al LDH synthesis

Mg–Al LDH nanoparticles were synthesized based on the co-precipitation method offered in the literature with slight modifications (Huang et al. 2019). Firstly, $\text{Mg}(\text{NO}_3)_2 \cdot 6\text{H}_2\text{O}$ and $\text{Al}(\text{NO}_3)_3 \cdot 9\text{H}_2\text{O}$ with an Mg:Al molar ratio of 3:1 were dissolved in 100-mL deionized water and the solution was named A. Secondly, solution B, which consisted of 200 mL of 0.583 M Na_2CO_3 and 1 M NaOH solution, was prepared. Solution A was then added to solution B under vigorous stirring while pH was maintained around 10. The resulting suspension was then heated at 65 °C for 18 h, filtered, washed, and dried at 80 °C for 24 h to form Mg–Al LDH nanoparticles.

HA/Mg–Al LDH nanocomposite synthesis

The HA/Mg–Al LDH nanocomposite was synthesized by adding 1 g of synthesized HA to 100 mL of as-prepared solution A, followed by sonication for 30 min in an ultrasonic bath. Afterward, solution B, with the same ratios as in Mg–Al LDH synthesis, was added to the suspension of HA and solution A, stirred for 24 h, aged at 65 °C, and then filtered and rinsed to neutralize. Finally, the white nanocomposite was dried at 110 °C for 24 h, ground, and stored in a

Table 1 The physicochemical features of three different anionic dyes

| Pollutant | Chemical formula (Mol. Wt. in g/mol) | Structure |
|------------------|--|--|
| Alizarin Red S | $\text{C}_{14}\text{H}_7\text{NaO}_7\text{S}$ (342.26) |  |
| Congo Red | $\text{C}_{32}\text{H}_{22}\text{N}_6\text{Na}_2\text{O}_6\text{S}_2$ (696.66) |  |
| Reactive Red 120 | $\text{C}_{44}\text{H}_{24}\text{Cl}_2\text{N}_{14}\text{Na}_6\text{O}_{20}\text{S}_6$ (1469.34) |  |

desiccator. Figure S2 presents a scheme of the HA/Mg–Al LDH nanocomposite synthesis procedure.

Characterization and instruments

Phase analysis of the nanocomposite was conducted using X-ray diffraction (XRD) (PANalytical X'Pert Pro Alpha) with CoK_α irradiation ($\lambda = 0.17809$ nm at 40 kV and 30 mA, 2θ ranging from 10 to 70°). Surface morphology and elemental composition were assessed through SEM (Hitachi S-4800) with energy-dispersive X-ray spectrometry (EDS). The size and shape of the nanocomposites were determined using Hitachi H-7600 transmission electron microscopy (TEM). To provide a typical statistical size distribution, the particle size was estimated using the software ImageJ and ellipses to redraw and admeasure particles. An Attenuated Total Reflectance Fourier Transform Infrared (FTIR–Bruker Vertex 70) in a spectral range of 400–4000 cm^{-1} was used for surface group identification. Anionic dye concentrations (ARS, CR, and RR 120) were determined via a Spectrum SP-UV 300SRB UV–visible spectrophotometer at their respective λ_{max} values (423 nm, 498 nm, and 516 nm, respectively). The zeta potential of the adsorbent was measured by the Zetasizer Nano ZS instrument. The N_2 adsorption–desorption analysis (Tristar® II plus) was performed to obtain the Brunauer–Emmett–Teller (BET) specific surface area and pore size of the adsorbent.

Adsorption studies

Adsorption studies investigated the effect of adsorption dosage (0.1–5 g/L), pH (3–12), contact time (10–240 min), temperature (20–40 $^\circ\text{C}$), and initial dye concentration (5–500 ppm) on the adsorption efficiency and capacity of synthesized adsorbents. Considering all three dyes, the ranges of the experimental parameters were carefully determined based on previous literature (Rapo and Tonk 2021), preliminary experiments, and the nature of the study. In a typical experiment, 10 mL of dye solution and 5 mg of adsorbent were mixed in a 15-mL tube using a Lab Teamet Shaker at 200 rpm. pH adjustment was done with 0.1 M HCl and 0.1 M NaOH for initial dye solutions. After the adsorption experiment, the dye solution was filtered through 0.2- μm Minisart RC syringe filters to separate the adsorbents, and the filtrate determined the final dye concentration. Dye adsorption efficiency (%) and capacity (mg/g) were calculated using the following equations:

$$R = 1 - \frac{C_o}{C_e} \quad (1)$$

$$q_e = \frac{V(C_o - C_e)}{m} \quad (2)$$

where C_o and C_e are the initial and final dye concentrations, V is the volume of the dye solution, and m is the mass of adsorbent. Dye concentration at any time (C_t) was also measured to investigate the effect of contact time and kinetic adsorption. In a typical experiment, $C_o = 50$ ppm, $V = 10$ mL, $m = 5$ mg, and 120 min contact time were employed.

Regeneration of nanoadsorbents

The regeneration study was performed in the batch mode similar to adsorption tests. Firstly, 10 mg of the adsorbent was immersed in 10-mL dye solution ($C_o = 100$ ppm) in the optimum condition and stirred for 4 h to reach an equilibrium. Secondly, the adsorbents were collected, washed with deionized water to remove surface dye molecules, and then immersed in 0.1 M NaOH, Na_2CO_3 , and methanol solutions. Afterward, they were thoroughly washed with deionized water to eliminate unreacted agents and neutralize. Finally, the regenerated adsorbents were dried at 60 $^\circ\text{C}$ for 12 h and used in adsorption studies. This adsorption–desorption cycle was repeated five times to assess the reusability of adsorbent in dye removal and measure dye adsorption efficiency.

Results and discussion

Characterization of nanoadsorbents

XRD results for the synthesized nanoadsorbents are shown in Fig. 1a. HA nanoparticles exhibit characteristic peaks matching the crystallographic information of hydroxyapatite (ICSD code 1–072–1243) (Pereira Rocha et al. 2021). The main diffraction peaks are also depicted in the figure (Boujaady et al. 2016; Googerdchian et al. 2018; Harja and Ciobanu 2018). According to Scherrer's formula ($D = \frac{0.9\lambda}{\text{FWHM} \cdot \cos\theta}$) (Mahmoodi et al. 2018), the HA particles have crystal sizes in nanorange (maximum crystal size of 30.6 nm for the (211) reflection peak). The XRD pattern of Mg–Al LDH nanoparticles corresponds to hydrotalcite sheet-like materials (ICSD 98–0000–6296). Using the first diffraction peak indexed as (003), the basal spacing was determined to be 0.776 nm. Assuming a thickness of 0.477 nm for the hydrotalcite layer (Muráth et al. 2017), the interlayer spacing of Mg/Al LDH was calculated to be 0.299 nm, which aligns closely with the literature value of 0.312 nm (Huang et al. 2019). Furthermore, the calculation yielded a crystallite size of 25.6 nm, confirming the nanostructure of the Mg–Al LDH. The strong, narrow diffraction peaks indicate well-crystallized and larger microcrystalline sizes for the synthesized Mg–Al LDH, including carbonate ((003), (006), and (009)) intercalated Mg–Al LDH in the R3m space group (Naseem et al. 2020). The XRD pattern of HA/Mg–Al LDH nanocomposite shows the characteristic

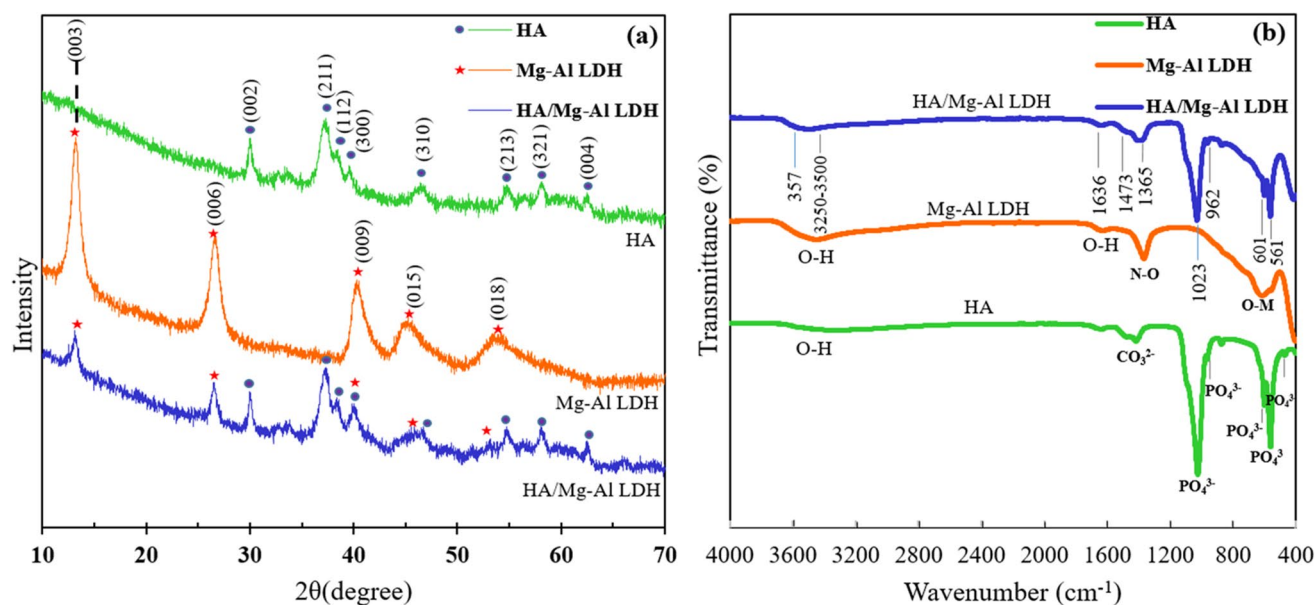


Fig. 1 **a** XRD pattern and **b** FTIR spectra of HA, Mg-Al LDH, and HA/Mg-Al LDH nanoadsorbents

peaks of both HA and Mg-Al LDH, confirming the composite structure and the mediation of sharp peaks in the Mg-Al LDH pattern due to HA addition (Fayyazbakhsh et al. 2017).

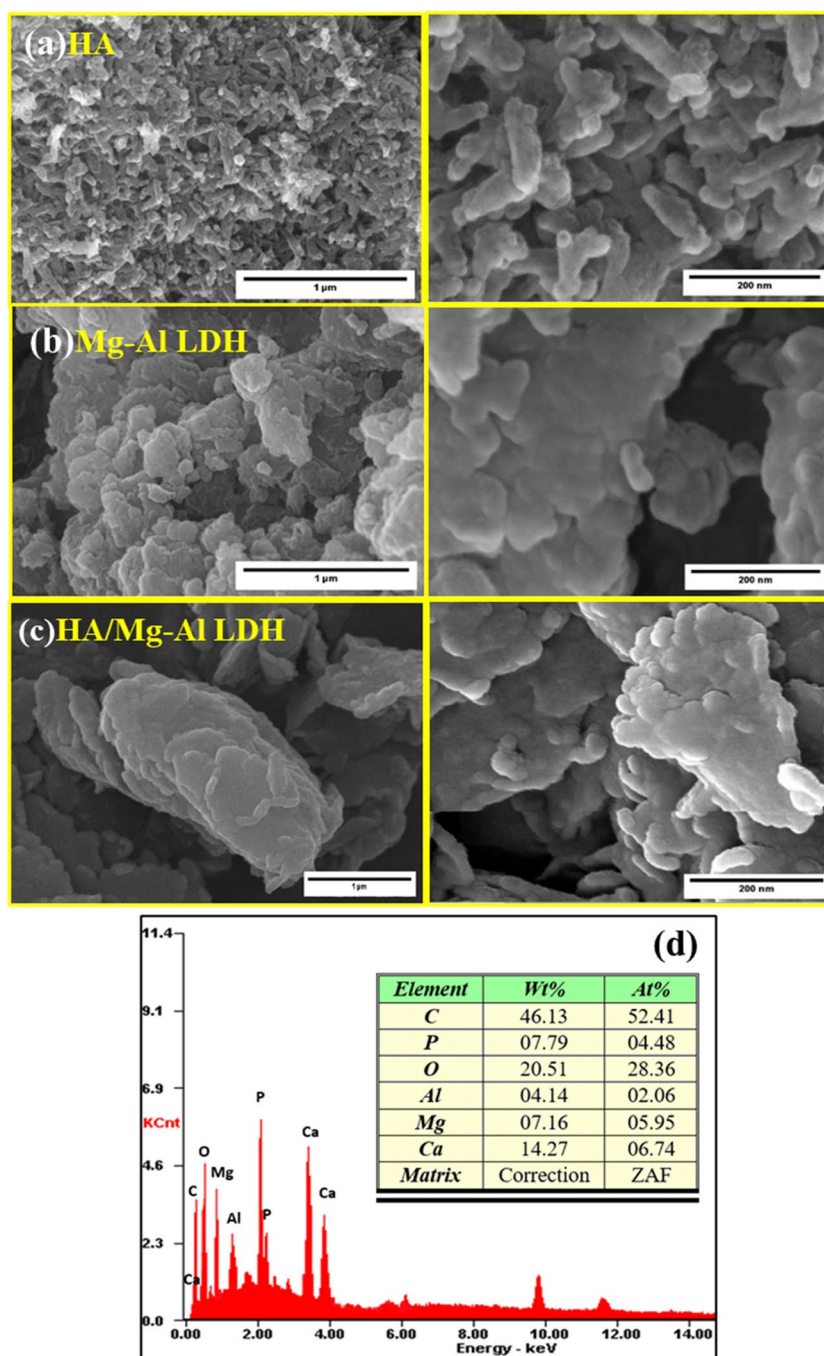
The FTIR spectra of the as-synthesized nanomaterials are shown in Fig. 1b. Concerning HA nanoparticles, the broadband at around 3570 cm^{-1} signifies O-H stretching vibration and hydrogen bonding. The 1636 cm^{-1} band corresponds to intercalated water in HA layers. Phosphate groups are confirmed at 1023, 962, 601, 561, and 470 cm^{-1} , while the 1473 cm^{-1} band denotes carbonate ions (Klinkaewnarong et al. 2009). In the case of Mg-Al LDH, the $3250\text{--}3500\text{ cm}^{-1}$ broadband represents O-H stretching in $\text{Al}(\text{OH})_3$ and $\text{Mg}(\text{OH})_2$ layers. The 1630 cm^{-1} band reflects O-H bending vibration due to water deformation in the interlayer domain. The presence of nitrate group (N-O bending) is confirmed at 1365 cm^{-1} , and lattice vibration modes of M-OH and M-O can be observed between 400 and 900 cm^{-1} (Ai et al. 2011). The presence of characteristic peaks for HA and Mg-Al LDH confirms the well-prepared nanocomposite. The band intensity of HA's phosphate and Mg-Al LDH's nitrate groups was diminished because of nanocomposite formation. The intercalation of HA's phosphate group into the interlayer spaces of Mg-Al LDH, along with the ion exchange involving nitrate ions, can result in the presence of phosphate in both phases (Fayyazbakhsh et al. 2017).

Figure 2 shows the SEM image of the nanoadsorbents. In Fig. 2a, synthesized HA nanoparticles are observed as nanorods with radii around 30 nm and an average height of 150 nm, a common morphology for HA nanoparticles (Harja and Ciobanu 2018). Figure 2b shows typical stacked LDH particles with the sheet layers in submicron

size. Figure 2c displays the HA/Mg-Al LDH nanocomposite with smaller Mg-Al LDH layers due to the presence of HA acting like a support on which Mg-Al LDH nanoparticles could form freely and separately. As a result, the stacked layers of Mg-Al LDH were substituted with delaminated Mg-Al LDH layers in contact with HA nanoparticles. SEM images confirm that all synthesized adsorbents have dimensions in the nanometer range, with at least one dimension below 100 nm. Additionally, Fig. 2d displays EDS analysis of the HA/Mg-Al LDH composite, providing a clear endorsement of its surface components. The Mg and Al elements are visible, along with oxygen, corresponding to hydroxide bonds in the LDH structure. Furthermore, the presence of Ca and P on the surface confirms the accuracy of HA synthesis.

The morphology of the synthesized nanoadsorbents was further investigated using TEM images. Figure 3a reveals the nanorod shape of HA nanoparticles with an average particle size of 82.3 nm. In Fig. 3b, the stacked structure of Mg-Al LDH particles makes it challenging to discern individual layers, with darker areas representing multiple stacked layers and nearly transparent areas showing single layers. Figure 3c confirms the presence of both HA and Mg-Al LDH nanoparticles in the HA/Mg-Al LDH nanocomposite with an average particle size of 77.3 nm. Separate Mg-Al LDH particles in a monolayer sheet structure are evident, and their size does not exceed 100 nm, indicating potential surface availability for adsorption. The Mg/Al LDH nanoparticles are in hexagonal structures, consistent with prior studies, though the size of LDH sheets is smaller in our work (Xiong et al. 2019).

Fig. 2 SEM images of the nanoadsorbents: **a** HA, **b** Mg–Al LDH, and **c** HA/Mg–Al LDH, and **d** EDS analysis of the nanocomposite



Nitrogen adsorption–desorption analysis was conducted at 77 K after overnight degassing at 105 °C to remove moisture and volatile substances that could affect adsorption experiments. The results were reported in the relative pressure range of $1.0 \times 10^{-2} < P/P_0 < 1.0$. Additionally, pore size distribution was determined using the Barrett–Joyner–Halenda (BJH) method. The isotherm in Fig. 4 and its BJH pore size distribution show type IV adsorption isotherms for the nanocomposite, indicating mesoporous characteristics. The hysteresis curve also confirms the

mesoporous structure with fairly open tubular-shaped pores. The BJH pore size distribution ranging from 2 to 40 nm further confirms the presence of a mesoporous structure in the nanocomposite.

The Brunauer–Emmett–Teller (BET) surface area measurement was used to assess the availability of adsorption sites for the nanoadsorbents. Table 2 confirms that most of the pores were in the mesopore range, with only a small proportion in the micropore range. The HA/Mg–Al LDH had the highest BET surface area at 111.19 m²/g, followed

Fig. 3 TEM and particle size distribution images of the nanoadsorbents: **a** HA, **b** Mg–Al LDH, **c**, **d** HA/Mg–Al LDH nanocomposite at 200-nm and 50-nm magnification

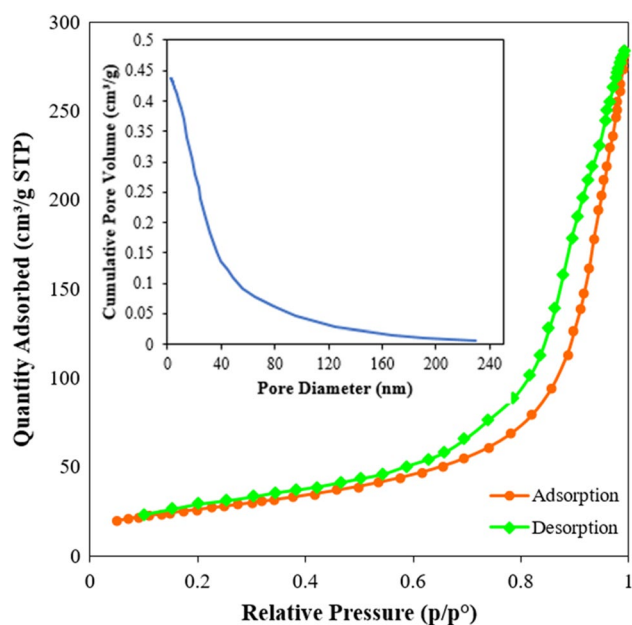
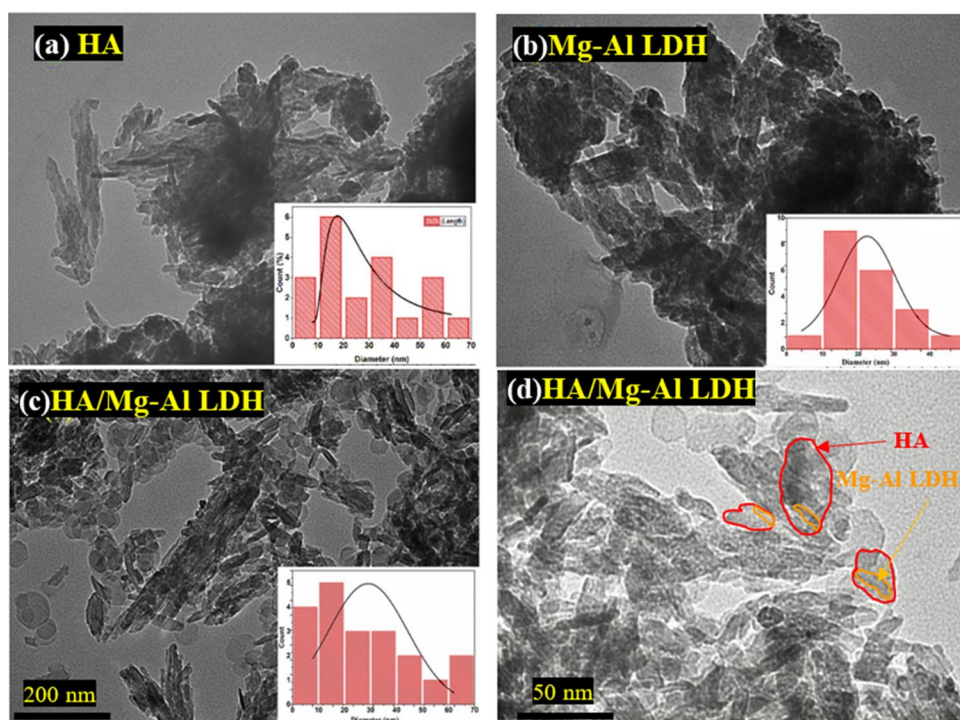


Fig. 4 N_2 adsorption/desorption isotherms and BJH pore size distribution of the mesoporous HA/Mg–Al LDH nanocomposite

by HA at $105.03 \text{ m}^2/\text{g}$ and Mg–Al LDH at $93.63 \text{ m}^2/\text{g}$. The higher specific surface area of the HA/Mg–Al LDH nanocomposite compared to Mg–Al LDH can be attributed to its exfoliated structure as confirmed by TEM and SEM. Results from the average particle size of the nanoadsorbents further support their nanoscale structure. The HA/Mg–Al

LDH nanocomposite had the smallest average particle size at 53.96 nm , while Mg–Al LDH had the largest at 64.08 nm . The average particle size obtained from BET analysis aligns well with the estimated average particle size from TEM images.

Adsorption studies

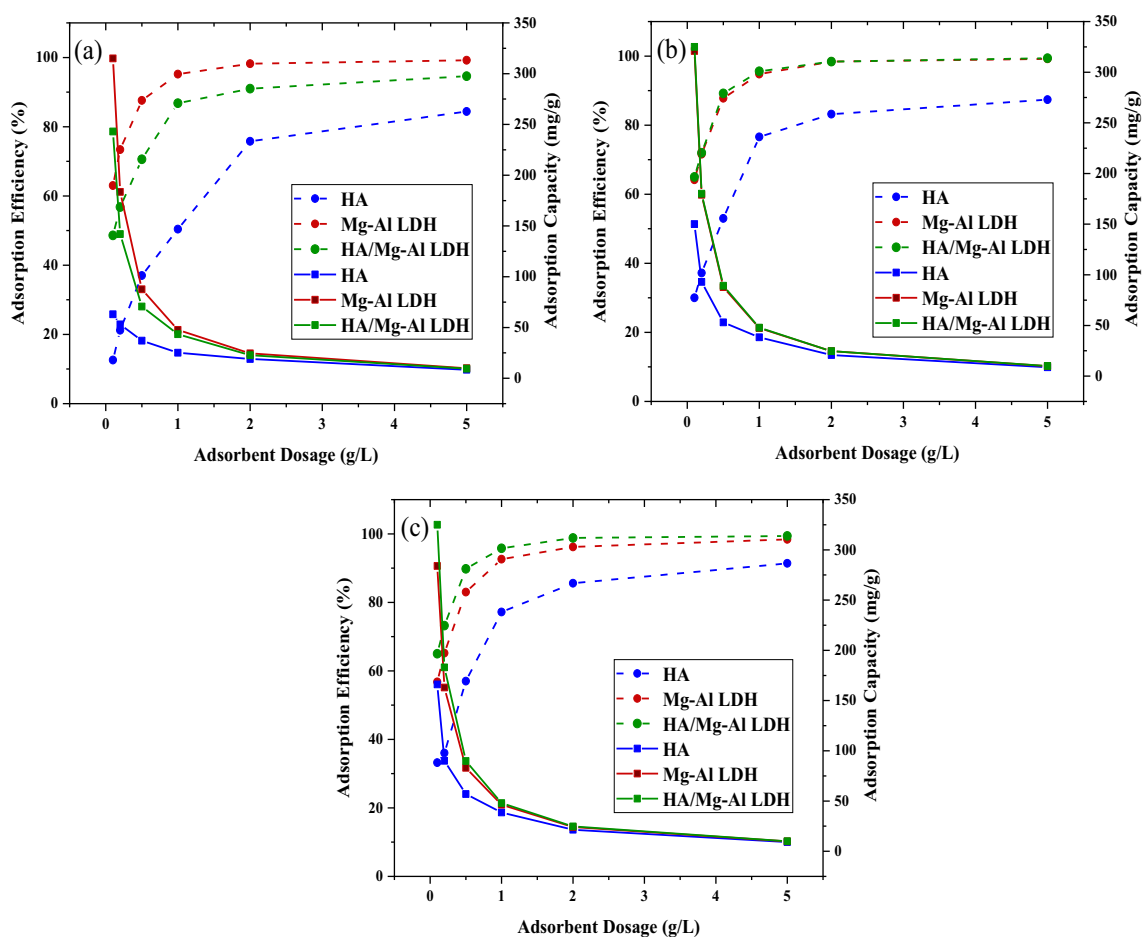
Effect of adsorbent dosage

The effect of sorbent dosage on adsorption efficiency and capacity of the nanoadsorbents is shown in Fig. 5. The adsorbent dosage was varied between 0.1 and 5 g/L . With increasing dosage, adsorption efficiency rises, while adsorption capacity decreases. This is due to the availability of more adsorption sites at higher dosages. At low dosages, the increase in efficiency and decrease in capacity are more pronounced as there are plenty of available adsorption sites (Tanhaei et al. 2015). As the dosage increases, most dye molecules are already adsorbed, leaving some sites unoccupied.

HA nanoparticles at the highest dosage adsorbed 84.4% , 87.4% , and 91.4% of ARS, CR, and RR120, respectively. In contrast, Mg–Al LDH and HA/Mg–Al LDH nanocomposite nearly completely adsorbed all three dyes. Mg–Al LDH was highly effective with ARS, while HA/Mg–Al LDH excelled with RR120. HA was far less efficient than Mg–Al LDH for ARS and CR, which can be the reason for the lower adsorption of HA/Mg–Al LDH nanocomposite. However, as the gap between the

Table 2 BET analysis results of the nanoadsorbents

| Samples | $S_{\text{BET}}^{\text{a}}$ (m^2/g) | $S_{\text{ext}}^{\text{b}}$ (m^2/g) | D_{a}^{c} (nm) | V_{p}^{d} (cm^3/g) | V_{t}^{e} (cm^3/g) | S_{p}^{f} (nm) |
|--------------|---|---|--------------------------------|--|--|--------------------------------|
| HA | 105.03 | 100.74 | 10.492 | 0.275 | 0.00125 | 57.13 |
| Mg–Al LDH | 93.63 | 87.53 | 13.445 | 0.311 | 0.00230 | 64.08 |
| HA/Mg–Al LDH | 111.19 | 106.10 | 11.252 | 0.323 | 0.00161 | 53.96 |

^aBET specific surface area^bSpecific external surface area^cAverage pore diameter^dTotal pore volume^eMicropore volume calculated from t-method^fAverage particle size**Fig. 5** Effect of adsorbent dosage on dye adsorption efficiency (dashed line) and capacity (solid line): **a** ARS, **b** CR, and **c** RR120

dye adsorption capacity of HA and Mg–Al LDH narrows down while removing CR and RR 120, HA/Mg–Al LDH exhibits a better dye adsorption performance than the other two adsorbents. Furthermore, HA/Mg–Al LDH nanocomposite with more available layers compared to Mg–Al LDH (showed in SEM and TEM images and the BET surface area measurements) could slightly outperform HA and Mg–Al LDH in adsorbing CR and RR120. Dye removal plateaued at an adsorbent dosage exceeding 1 g/L.

A dosage of 0.5 g/L was chosen as the optimal level for subsequent experiments, providing relatively high adsorption efficiencies and capacities. Too high a dosage will result in low capacity and will not show the changes in adsorption efficiency by other parameters because it will be around 100%. Too low a dosage is also unsuitable because although adsorption capacity would be high, the adsorption efficiency would be too low, leading to high concentration of dyes in the treated dye solution.

Effect of dye solution pH

Figure 6 illustrates the impact of pH on anionic dye adsorption. Generally, dye molecules were readily adsorbed under acidic conditions, while high pH values resulted in poor dye capacity (Tanhaei et al. 2016). There was a significant gap in the adsorption capacity of HA and Mg–Al LDH nanoparticles toward ARS with only one SO_3^- group, while the gap for RR120 that possesses six SO_3^- groups was less significant. In addition, variations in dye removal capacity as a function of pH were more significant for HA compared to Mg–Al LDH, also affecting HA/Mg–Al LDH nanocomposite. This indicates that adsorption of anionic dyes onto HA was more pH-dependent, which may show that electrostatic adsorption between SO_3^- groups in the anionic dyes and the functional groups of the HA is more significant, whereas Mg–Al LDH nanoparticles tend to adsorb dyes through other adsorption mechanisms such as hydrogen bonding, chelation, and ion exchange (Daud et al. 2019).

Additionally, adsorption of ARS by the three nanoadsorbents experienced an almost downward trend throughout the pH range, with pH = 4 being the best condition. However, for CR and RR120, the most efficient pH was 5. These observations can be explained by determining the surface charge of the particles. Zeta potential measurements (Fig. 6d) revealed pH_{PZC} values (pH at which surface charge equals zero) for the nanoadsorbents, with HA at 6.9, Mg–Al LDH at 8.8, and HA/Mg–Al LDH at 8.3.

In the pH values below pH_{PZC} , the surface was positively charged, attracting anionic dyes on the adsorption sites, raising both adsorption efficiency and capacity. Conversely, at higher pH values, the negatively charged surface repelled the anionic dyes, reducing adsorption efficiency and capacity. However, a reduction in CR and RR120 dyes' adsorption capacity in highly acidic situations can be justified by the negative charge on the surface of the dyes. The pK_a value, as an indicator of the acidic strength of the dye, represents the point lower than which dye molecules protonate, acquiring

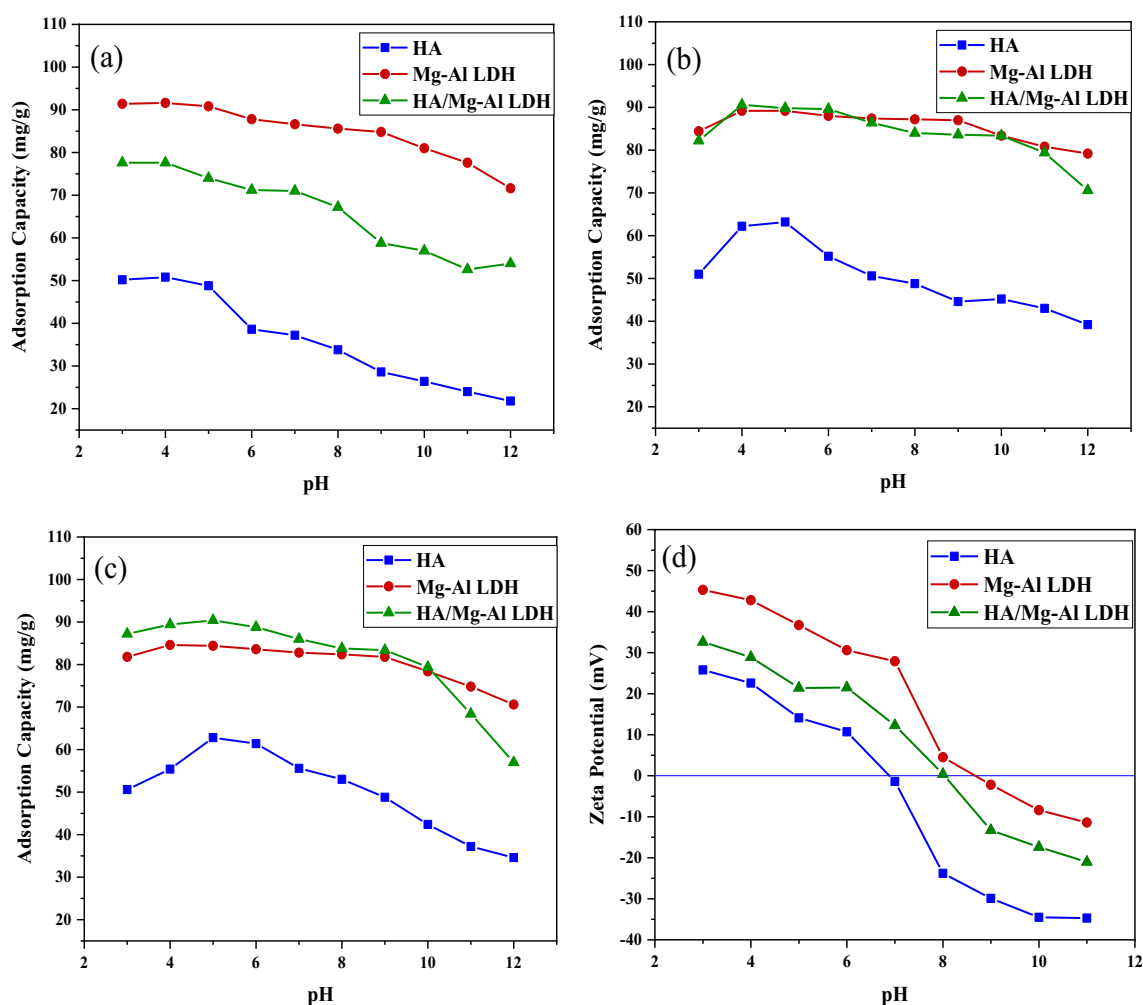


Fig. 6 Effect of initial pH of anionic dye solution on adsorption capacity of nanoadsorbents: **a** ARS, **b** CR, **c** RR120, and **d** zeta potential

a positive charge. According to the reported pK_a values for the dyes used in this work (4.1 for ARS, 4–5.5 for CR, and 4.4 for RR120) (Cotoruelo et al. 2010; Errais et al. 2012; Ghaedi et al. 2012; Wu et al. 2012), it can be concluded that overly acidic conditions reduced CR and RR120 dye adsorption due to the electrostatic repulsion between positively charged dye surfaces and positively charged nanoadsorbent surfaces. Considering these results, pH 5 was chosen for further experiments.

Effect of contact time

The effect of contact time on dye removal efficiency and capacity is presented in Fig. 7. As the contact time between the nanoadsorbents and the dyes increases, an overall increase is observed in adsorption capacity for all three nanoadsorbents, indicating that with extended contact times,

more dye molecules are adsorbed onto the nanoadsorbent surfaces. This behavior aligns with previous research findings (Tanhaei et al. 2015). However, the rate of dye removal diminishes as contact time extends, which is attributed to the decreasing availability of adsorption sites on the nanoadsorbent surfaces at longer contact times. It is observed that all three nanoadsorbents reach a nearly constant adsorption capacity after 120 min, so 120 min was considered the optimal contact time for subsequent stages. A significant observation is the variation in equilibrium times among the nanoadsorbents. HA nanoparticles achieve equilibrium faster than Mg–Al LDH nanoparticles. This discrepancy can be attributed to the compact structure and lower BET surface area of Mg–Al LDH, which hinders the transfer and adsorption of dye molecules. Consequently, in the case of HA/Mg–Al LDH nanocomposite, the equilibrium time is shorter than that of Mg–Al LDH. Similarly, adsorption capacity

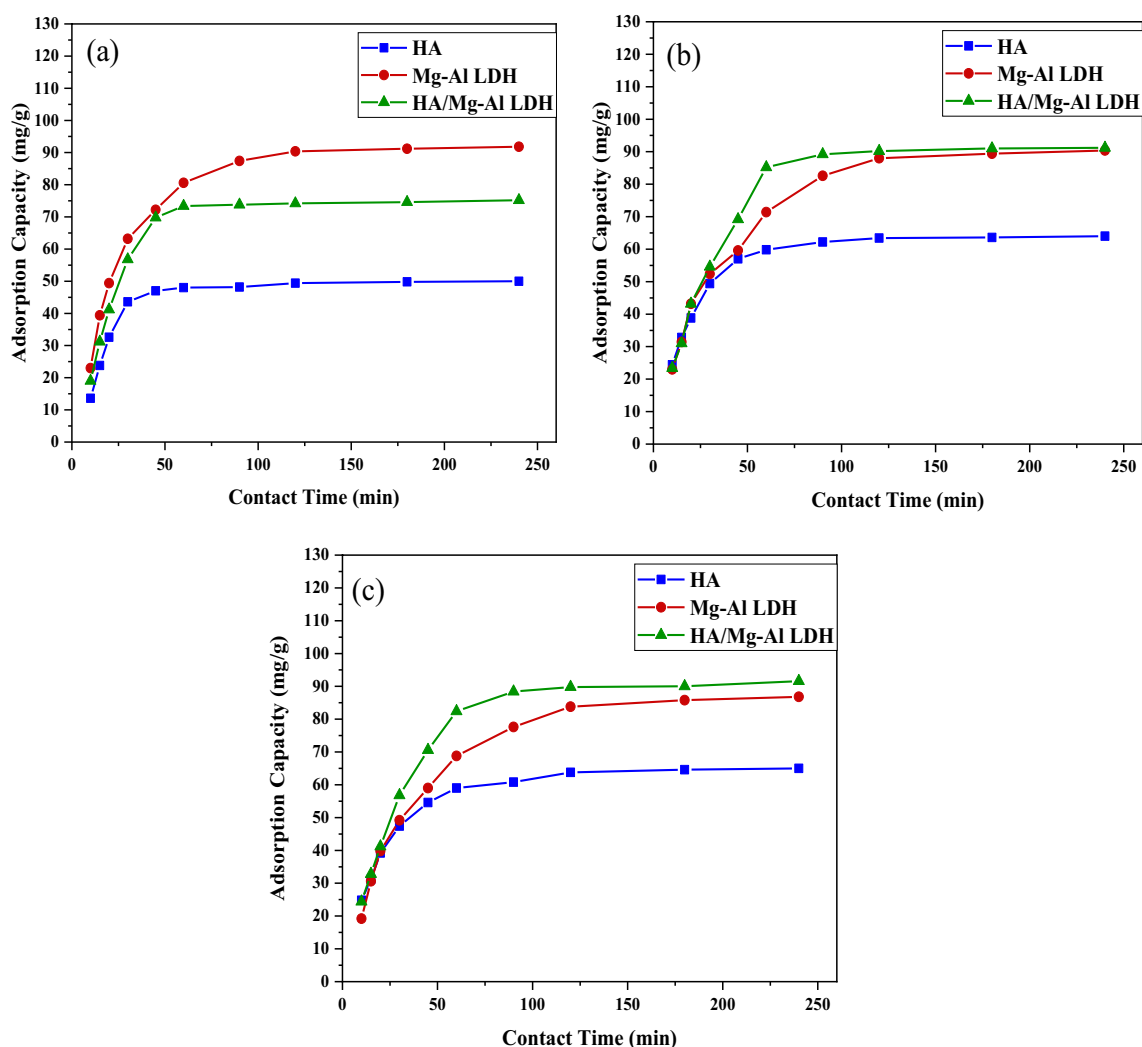


Fig. 7 Effect of contact time on adsorption capacity of nanoadsorbents: **a** ARS, **b** CR, and **c** RR120

Table 3 Parameters of kinetic models' study

| Adsorbent | Kinetic model | Parameters | ARS | CR | RR120 |
|--------------|-------------------------|---------------------------------------|---------|---------|---------|
| HA | First-order | Calculated q_e (mg/g) | 23.556 | 35.127 | 42.384 |
| | | k_1 (1/min) | 0.0126 | 0.0125 | 0.0119 |
| | | R^2 | 0.9012 | 0.9313 | 0.9804 |
| | Second-order | Calculated q_e (mg/g) | 53.763 | 68.493 | 69.930 |
| | | $k_2 \times 10^{-5}$ (g/(mg·min)) | 136.151 | 115.097 | 96.640 |
| | | R^2 | 0.9916 | 0.9940 | 0.9887 |
| | Intraparticle diffusion | k_{id} ((mg/g)/min ^{1/2}) | 2.339 | 2.92 | 3.073 |
| | | C (mg/g) | 21.702 | 27.949 | 26.217 |
| | | R^2 | 0.5785 | 0.7032 | 0.7623 |
| Mg–Al LDH | First-order | Calculated q_e (mg/g) | 72.127 | 84.411 | 81.583 |
| | | k_1 (1/min) | 0.0125 | 0.0113 | 0.0109 |
| | | R^2 | 0.9765 | 0.9837 | 0.9932 |
| | Pseudo-second-order | Calculated q_e (mg/g) | 102.041 | 104.167 | 101.010 |
| | | $k_2 \times 10^{-5}$ (g/(mg·min)) | 45.930 | 31.911 | 30.801 |
| | | R^2 | 0.9978 | 0.9959 | 0.9894 |
| | Intraparticle diffusion | k_{id} ((mg/g)/min ^{1/2}) | 5.105 | 5.555 | 5.424 |
| | | C (mg/g) | 27.617 | 18.262 | 16.242 |
| | | R^2 | 0.7644 | 0.8605 | 0.8582 |
| HA/Mg–Al LDH | First-order | Calculated q_e (mg/g) | 36.400 | 88.797 | 64.759 |
| | | k_1 (1/min) | 0.0122 | 0.157 | 0.109 |
| | | R^2 | 0.8104 | 0.9744 | 0.8919 |
| | Pseudo-second-order | Calculated q_e (mg/g) | 82.647 | 104.167 | 104.167 |
| | | $k_2 \times 10^{-5}$ (g/(mg·min)) | 68.608 | 37.312 | 38.177 |
| | | R^2 | 0.9987 | 0.9951 | 0.9922 |
| | Intraparticle diffusion | k_{id} ((mg/g)/min ^{1/2}) | 4.016 | 5.595 | 5.490 |
| | | C (mg/g) | 26.475 | 21.617 | 22.451 |
| | | R^2 | 0.6384 | 0.7641 | 0.7752 |

of HA/Mg–Al LDH was higher than that of Mg–Al LDH (except for ARS removal in Fig. 7b), showing the better performance of HA/Mg–Al LDH nanocomposite in adsorption of dye molecules containing more SO_3^- groups. These can be attributed to the formation of HA nanoparticles on the separate layers of LDH in the composite, corroborated by SEM and TEM analysis, and the lower BET surface area. It is worth noting that although in all three figures, Mg–Al LDH required a longer time to reach equilibrium, the final adsorption capacity of Mg–Al LDH nanoparticles was still high. This shows some other mechanisms than electrostatic adsorption (such as hydrogen bonding and chelation which may be slower in nature) can play a role in anionic dye adsorption onto Mg–Al LDH nanoparticles.

Pseudo-first-order (or Lagergren), pseudo-second-order, and intraparticle diffusion kinetic models were examined to investigate the best-fitted kinetic model. Lagergren's first-order kinetic model can be presented in linear form by the following equation:

$$\log(q_e - q_t) = \log q_e - k_1 t \quad (3)$$

where q_t and q_e are the adsorption capacity (mg/g) of the adsorbent at time t (min) and equilibrium, respectively. In this equation, k_1 is the first-order rate constant (1/min). By plotting $\log(q_e - q_t)$ against t , k_1 can be achieved.

Pseudo-second-order model can be expressed by the following equation:

$$\frac{t}{q_t} = \frac{1}{k_2 q_e^2} + \frac{t}{q_e} \quad (4)$$

where k_2 is the second-order rate constant (g/(mg·min)). The value of k_2 and q_e can be measured by plotting t/q_t against t .

The intraparticle kinetic model assumes the changes in adsorption rate according to the root of elapsed time:

$$q_t = k_{id} \cdot t^{1/2} + C \quad (5)$$

where k_{id} is the intraparticle diffusion rate constant ((mg/g)/min^{1/2}), which can be associated with the thickness of the boundary layer.

The calculated parameters of kinetic models together with their corresponding coefficients of determination (R^2) values for different nanoadsorbents and dyes are

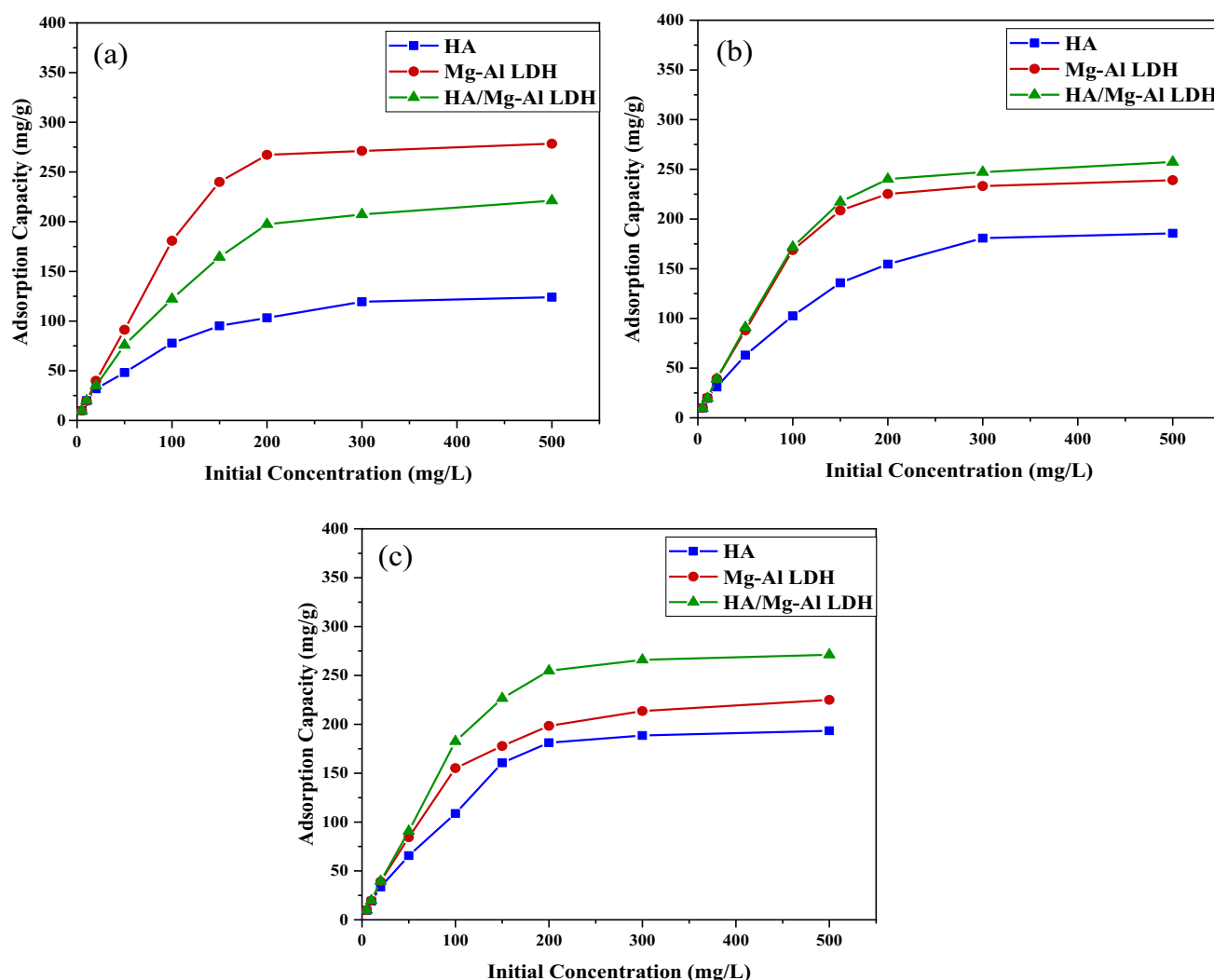


Fig. 8 Effect of initial anionic dye concentration on adsorption capacity of nanoadsorbents: **a** ARS, **b** CR, and **c** RR120

tabulated in Table 3. It shows that the pseudo-second-order kinetic model was the best model for all different dyes and nanoadsorbents, reflected in higher R^2 values. It was reported that this model can fit the data for an extended period, while the pseudo-first-order kinetic model predicts the data for a limited amount of time or when the adsorption is very fast (Haro et al. 2017). The intraparticle diffusion model does not follow a linear shape (figures are not presented here), suggesting that the intraparticle diffusion mechanism is not the sole rate-controlling mechanism of adsorption (Hosseini et al. 2011).

Effect of initial concentration

The impact of initial anionic dye concentration on dye adsorption capacity is presented in Fig. 8.

Generally, the dye removal capacity grows with an increase in dye concentration (Fig. 8). This can be related to the number of dye molecules that are available per adsorption site offered by higher dye concentration. Figure 8 also shows that the highest dye removal capacity is different for adsorbents. HA adsorbent possesses the lowest adsorption capacity of 124 mg/g when the maximum ARS dye concentration of 500 mg/g is applied. For the low molecular weight dye (i.e., ARS), the adsorption capacity of Mg/Al LDH is the highest at 278.4 mg/g, followed by HA-Mg/Al LDH nanocomposite with 221.2 mg/g. This trend is reversed with higher molecular weight dyes (CR and RR120), making HA-Mg/Al LDH the most efficient with an adsorption capacity of as high as 271.2 mg/g for RR120. This trend can again be justified with the fact that HA nanoparticles can adsorb through electrostatic adsorption of SO_3^- groups onto positively charged adsorption sites, while Mg/Al LDH nanoparticles also adsorb

Table 4 Isotherm parameters of anionic dye adsorption by nanoadsorbents

| Adsorbent | Kinetic model | Parameters | ARS | CR | RR120 |
|-----------|---------------|-----------------------------------|---------|---------|---------|
| HA | Langmuir | Calculated q_m (mg/g) | 128.205 | 208.333 | 222.222 |
| | | K_L (L/mg) | 0.0456 | 0.0517 | 0.0939 |
| | | R^2 | 0.9875 | 0.9654 | 0.9942 |
| | | | | | |
| | Freundlich | $K_f [(mg/g) \cdot (L/mg)^{1/n}]$ | 24.690 | 25.184 | 21.865 |
| | | n | 7.358 | 5.672 | 4.860 |
| | | R^2 | 0.9469 | 0.9686 | 0.9765 |
| | | | | | |
| | Langmuir | Calculated q_m (mg/g) | 344.828 | 277.778 | 256.410 |
| | | K_L (L/mg) | 0.0453 | 0.0615 | 0.1317 |
| | | R^2 | 0.9907 | 0.9836 | 0.9787 |
| | | | | | |
| Mg–Al LDH | Freundlich | $K_f [(mg/g) \cdot (L/mg)^{1/n}]$ | 31.741 | 29.309 | 24.204 |
| | | n | 5.148 | 5.063 | 4.689 |
| | | R^2 | 0.9591 | 0.9675 | 0.9757 |
| | | | | | |
| | Langmuir | Calculated q_m (mg/g) | 256.410 | 312.500 | 333.333 |
| | | K_L (L/mg) | 0.1553 | 0.0626 | 0.0486 |
| | | R^2 | 0.9873 | 0.9956 | 0.9727 |
| | | | | | |
| | Freundlich | $K_f [(mg/g) \cdot (L/mg)^{1/n}]$ | 28.669 | 28.977 | 24.891 |
| | | n | 5.716 | 4.904 | 4.334 |
| | | R^2 | 0.9585 | 0.9691 | 0.9734 |
| | | | | | |

anionic dyes through other mechanisms that can be more suitable for smaller dye molecules (ARS dye).

Langmuir and Freundlich isotherm models were used to study the adsorption behavior of adsorbents. Langmuir isotherm assumes a homogeneous monolayer adsorption, while there is no interaction between the dye and the adsorbent molecules, which is presented in the following linear form:

$$\frac{C_e}{q_e} = \frac{1}{K_L q_m} + \frac{C_e}{q_m} \quad (6)$$

where C_e (mg/L) is the equilibrium concentration of dye, K_L (mg/L) is the Langmuir equilibrium constant, and q_e (mg/g) and q_m (mg/g) are the adsorption capacity at equilibrium and the theoretical maximum adsorption capacity, respectively. The separation factor R_L was attained from the following equation:

$$R_L = \frac{1}{1 + K_L \cdot C_0} \quad (7)$$

where C_0 was the highest initial dye concentration (500 ppm in this work).

The Freundlich isotherm assumes a multilayer adsorption on a heterogeneous surface, which can be used in linear form as follows:

$$\ln(q_e) = \ln(K_F) + \frac{1}{n} \ln(C_e) \quad (8)$$

where $K_F [(mg/g) \cdot (L/mg)^{1/n}]$ and n are Freundlich isotherm constants. High K_F value is associated with high adsorption

capacity, and n value shows the heterogeneity of the surface. Typically, n values in different ranges of $n < 1$, $1 < n < 2$, and $2 < n < 10$ can be associated with poor, difficult, and good adsorption, respectively.

The correlation coefficients and isotherm constants of the Langmuir and Freundlich isotherms are listed in Table 4. As the regression coefficients of the linear plots show, the Langmuir isotherm can effectively predict the effect of initial anionic dye concentration on the adsorption capacity. The highest R^2 values for the Langmuir and the Freundlich isotherms were 0.9956 and 0.9765, respectively, which confirms that the Langmuir isotherm can be used with more precision. This shows that the adsorption of dye molecules is completed after the formation of a monolayer of dye molecules on the surface of the adsorbent (Ma et al. 2018). The maximum adsorption capacity values calculated from the Langmuir isotherm were very close to the values acquired from the experimental data in higher dye concentrations, further proving the suitability of the Langmuir isotherm. The separation factor constant (R_L) was used to further investigate the extent of favorability of the dye adsorption on the adsorbents. Unfavorable, linear, favorable, and irreversible adsorptions can be related to the R_L constants of $R_L > 1$, $R_L = 1$, $0 < R_L < 1$, and $R_L = 0$, respectively (Srivastava et al. 2018). The R_L values that were obtained for the adsorption of dyes by different nanoadsorbents varied from 0.0127 to 0.0423, indicating that the adsorption of dyes by nanoadsorbents was favorable. The n values from the Freundlich isotherm were in the range of 4.334–7.358, also indicating that the adsorption was favorable.

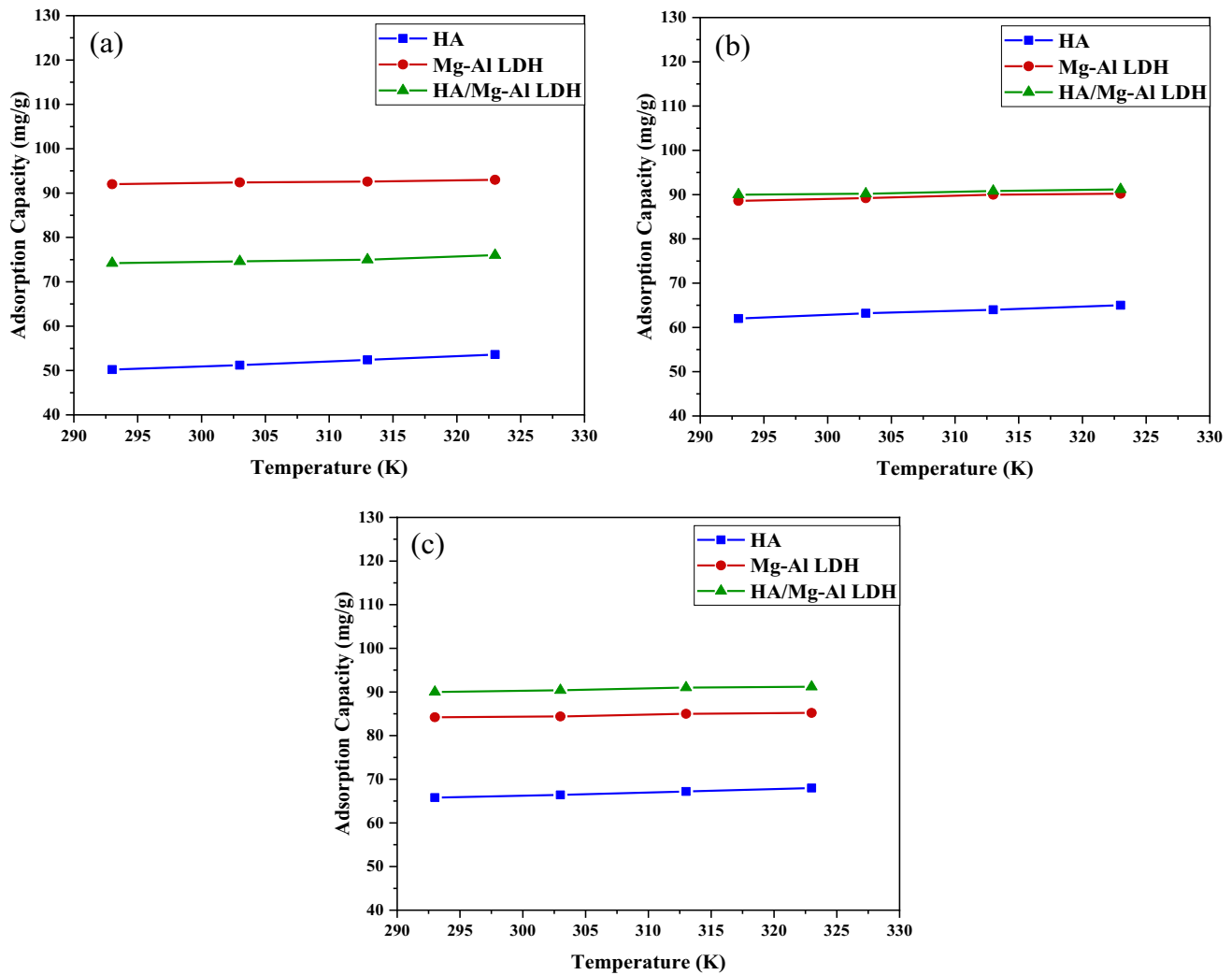


Fig. 9 Effect of temperature on dye adsorption capacity: **a** ARS, **b** CR, and **c** RR120

Effect of temperature

Figure 9 shows the effect of temperature on dye adsorption. An upward trend in dye adsorption capacity with temperature can be seen which showed the positive impact of temperature on dye adsorption by the three adsorbents, indicating the process is endothermic in nature, which can be due to faster diffusion of dye molecules in the solution at high temperatures (Huang 2017).

Thermodynamic parameters such as the change in Gibbs free energy (ΔG°), enthalpy (ΔH°), and entropy (ΔS°) were employed to measure intrinsic energy changes through adsorption (Srivastava et al. 2015):

$$k_c = \frac{C_{ad}}{C_e} \quad (9)$$

$$\Delta G^\circ = -RT \ln(k_c) \quad (10)$$

$$\Delta H^\circ = R \left(\frac{T_2 T_1}{T_2 - T_1} \right) \ln \left(\frac{k_{c2}}{k_{c1}} \right) \quad (11)$$

Table 5 Thermodynamic parameters of dye adsorption by nanoadsorbents

| Adsorbent | Parameters | ARS | CR | RR120 |
|--------------|----------------------------|----------|----------|----------|
| HA | ΔG° (J/mol) | −130.15 | −1305.70 | −1725.50 |
| | ΔH° (J/mol) | 3597.44 | 3393.10 | 2630.35 |
| | ΔS° (J/mol·K) | 12.26 | 15.66 | 14.336 |
| Mg–Al LDH | ΔG° (J/mol) | −6272.60 | −5343.9 | −4281.00 |
| | ΔH° (J/mol) | 3804.21 | 3841.98 | 2030.75 |
| | ΔS° (J/mol·K) | 33.23 | 32.19 | 20.820 |
| HA/Mg–Al LDH | ΔG° (J/mol) | −2715.50 | −5634.00 | −5674.10 |
| | ΔH° (J/mol) | 2589.32 | 3755.06 | 3674.77 |
| | ΔS° (J/mol·K) | 17.40 | 30.90 | 30.896 |

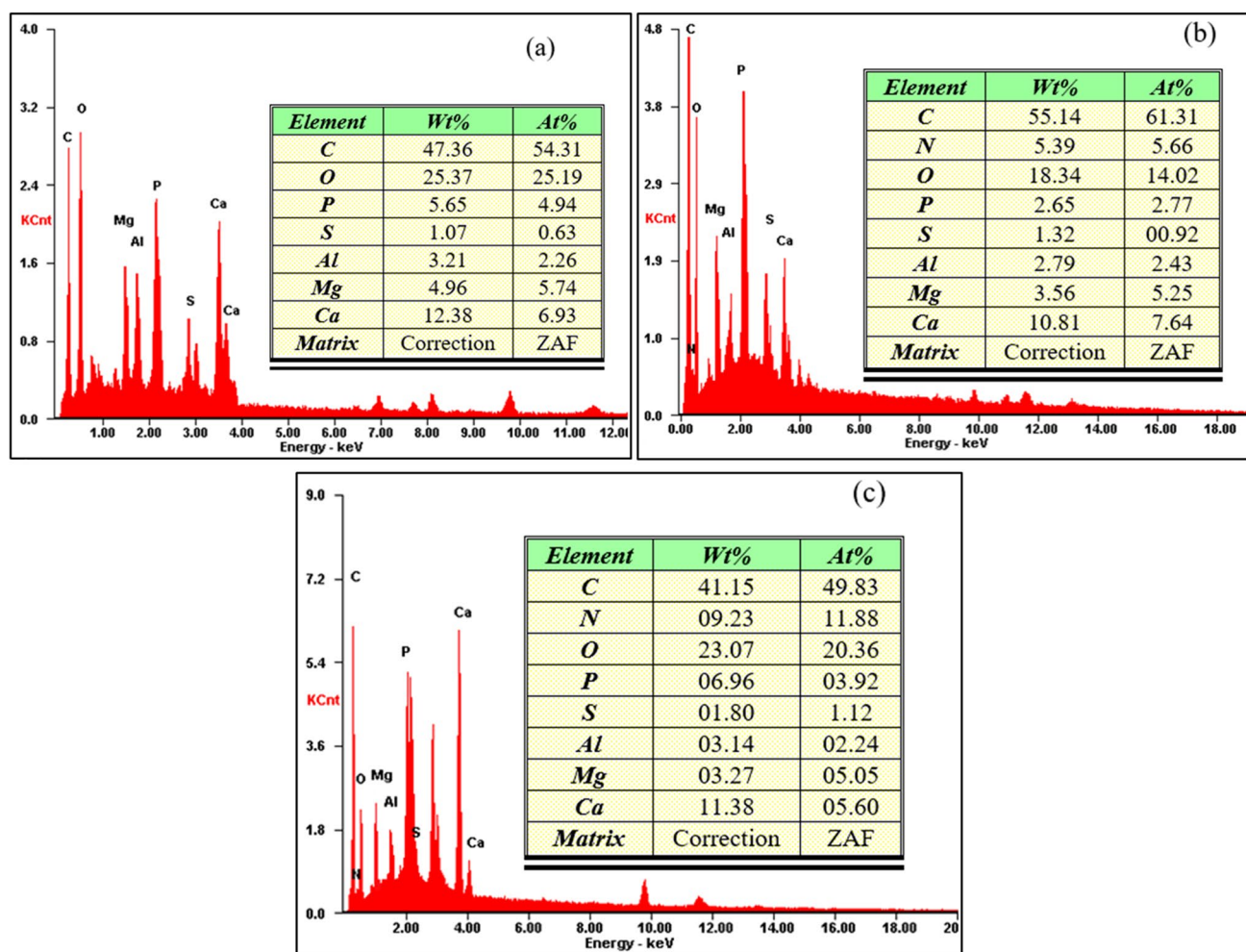


Fig. 10 EDS spectrum of HA/Mg–Al LDH nanocomposite after adsorption of **a** ARS, **b** CR, and **c** RR120

$$\Delta S^\circ = \frac{(\Delta H^\circ - \Delta G^\circ)}{T} \quad (12)$$

where k_c is the equilibrium constant, C_{ad} is the dye concentration adsorbed by the adsorbent, and C_e is the concentration of dye in the solution after dye adsorption. T_2 and T_1 are the higher and the lower temperatures, R is the gas constant (8.314 J/mol·K), and k_{c2} and k_{c1} are values corresponding to the higher and lower temperature. Table 5 shows the average values of thermodynamic parameters in the temperature range for the adsorption of different anionic dyes.

Positive values for the enthalpy change during the adsorption confirm the endothermic nature of the process. This shows that the energy required for dehydration is more than the energy released in the adsorption process, resulting in a net positive value for enthalpy change (Saha and Chowdhury 2011). As the values for enthalpy changes were all lower than the threshold for chemisorption (less than 40 kJ/mol), it can be perceived that the adsorption of

anionic dyes on the adsorbents is physical (Gusain et al. 2014). The negative ΔG° (J/mol) values suggest spontaneous adsorption that starts without an external source of energy (Zeynali et al. 2023). The positive values for ΔS° show the randomness of the process increases when adsorption takes place (Inglezakis and Zorpas 2019).

Characterization after adsorption

While the evident change in the color of nanocomposite to red as well as almost transparent solution confirmed dye adsorption, additional EDS analysis was conducted on the HA/Mg–Al LDH composite post-dye adsorption to explore and further confirm the adsorption process. Figure 10a–c presents the weight percentage (wt%) and atomic percentage (At%) of the elements present in the nanocomposite after the adsorption of ARS, CR, and RR-120, respectively. The figures reveal the composition of the nanocomposite,

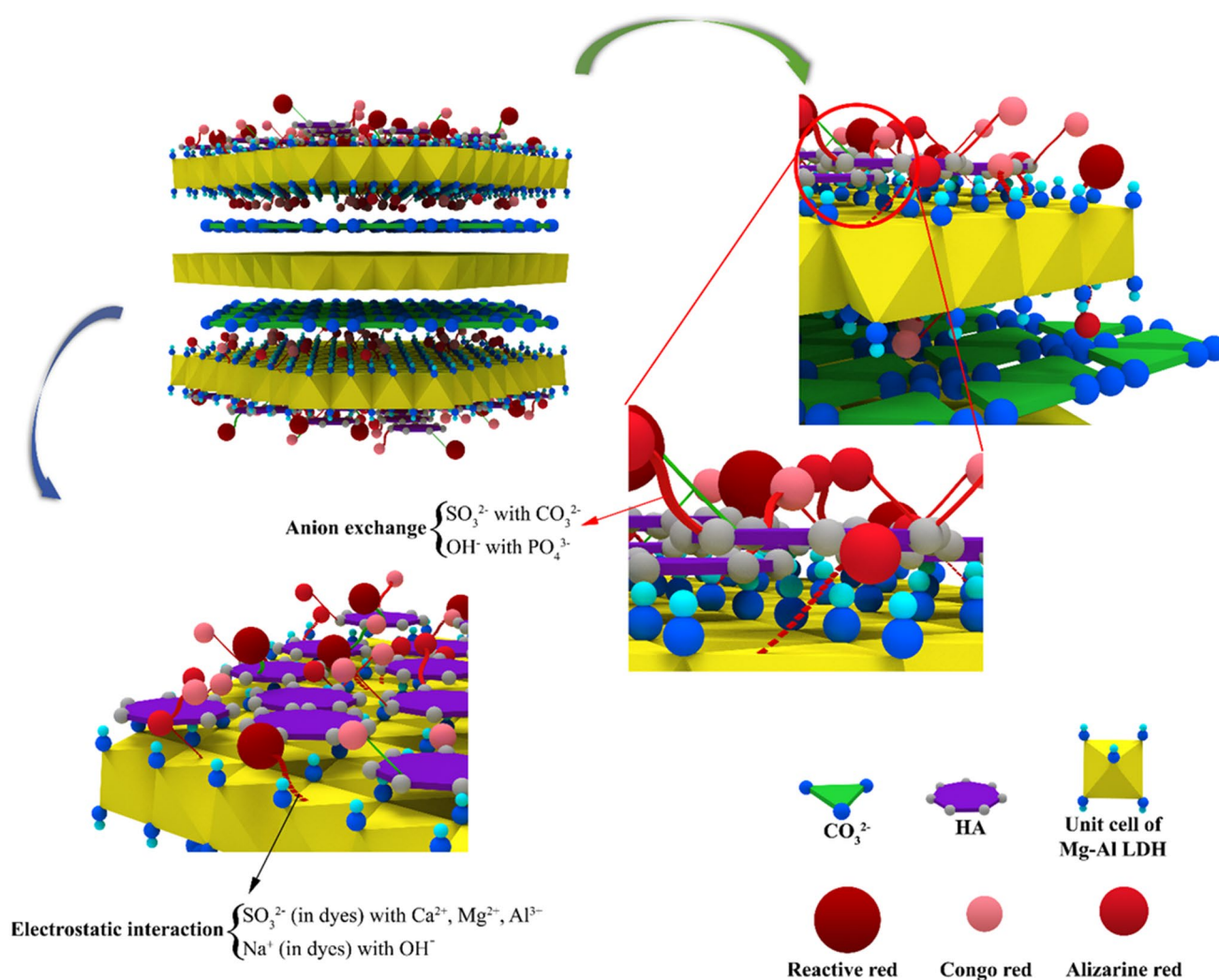


Fig. 11 Adsorption mechanism of HA/Mg-Al LDH for the removal of ARS, CR, and RR120

comprising elements Ca, P, Mg, Al, O, and C (as demonstrated in Fig. 2d), with traces of N and S. The detection of sulfur and nitrogen in the nanocomposite after dye adsorption provides additional confirmation of dye adsorption by the nanocomposite adsorbent. The higher atomic percentage of S in the adsorption of RR-120, associated with higher SO_3^- groups, provides a more detailed description of the enhanced adsorption of this dye on the nanocomposite surface.

Adsorption mechanism

Physical adsorption, electrostatic interaction between species with different charges, chemical bonding, and hydroxide precipitation are reported as the most significant adsorption mechanisms in adsorption by LDH nanoparticles and nanocomposites containing LDH (Daud et al. 2019). It has also been reported that the SO_3^- functional group of dyes can form a complex with

the surface metal ions of the LDH, leading to their adsorption on the LDH surface (Sheng et al. 2016). While complexation typically involves chemical reactions among different components, our thermodynamic findings indicate that the adsorption of dye molecules onto the nanoadsorbents primarily follows a physical adsorption process. The primary mechanism behind anionic dye adsorption by HA, Mg-Al LDH nanoparticles, and their nanocomposite seems to be physical adsorption rather than chemical complexation. This suggests that chemical complexation may not be the dominant factor contributing to the adsorption of anionic dyes by these materials. Hydrogen bonds between the OH groups in HA and Mg-Al LDH groups with electronegative residues (nitrogen and oxygen) in the dye structure can be another contributor to dye adsorption.

HA consistently exhibited lower adsorption capacity than Mg-Al LDH and HA/Mg-Al LDH nanocomposite, likely due to the higher intrinsic potential of Mg-Al LDH nanoparticles in anionic dye adsorption. Despite similar specific surface areas of

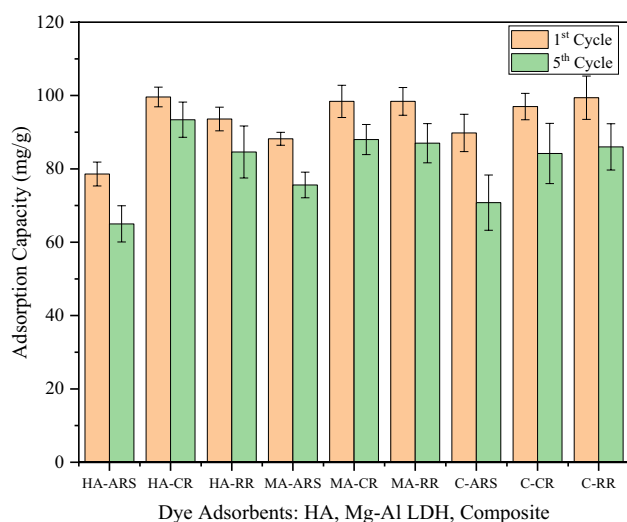


Fig. 12 Regeneration studies of nanoadsorbents in the first and fifth cycles for HA adsorbing ARS, CR, and RR120 (HA-ARS, HA-CR, HA-RR), Mg–Al LDH adsorbing ARS, CR, and RR120 (MA-ARS, MA-CR, MA-RR), and HA/Mg–Al LDH nanocomposite adsorbing ARS, CR, and RR120 (C-ARS, C-CR, C-RR)

the nanocomposites, factors other than physical adsorption contribute to the differences in their adsorption capacities. Examining dye removal capacity, it is evident that Mg–Al LDH's adsorption capacity decreases with an increase in the number of SO_3^- groups and molecular weight of dyes, contrary to the trend observed for HA and HA/Mg–Al LDH. This could be attributed to variations in the significance of distinct adsorption mechanisms. Mg–Al LDH nanoparticles took longer to reach adsorption equilibrium compared to the other two adsorbents, indicating potential diffusion challenges for dye molecules through the LDH layers. This hindrance in diffusion could explain the lower adsorption of RR120 in comparison to the lower-molecular-weight dye (less number of SO_3^- groups), as larger molecules face greater difficulty penetrating the layers in the Mg–Al LDH structure. The significant adsorption capacity of ARS by Mg–Al LDH can be attributed to the unimpeded flow of low-molecular-weight dyes between adsorbent layers. In contrast, HA exhibits its highest adsorption capacity with RR120, while the lowest capacity is linked to ARS, owing to the strong electrostatic attraction between HA adsorption sites and the SO_3^- functional groups of dyes. Considering the number of SO_3^- groups per molecule in the dyes used (1 SO_3^- group for ARS, 2 SO_3^- groups for CR, and 6 SO_3^- groups for RR120), it can be said that the higher number of SO_3^- groups in RR120 molecule is the reason for better adsorption of this dye by HA nanoparticles.

The HA/Mg–Al LDH nanocomposite implements both of the abovementioned mechanisms to adsorb anionic dyes, which is why it can adsorb CR and RR120 more than the other two nanoadsorbents. Apart from that, the delaminated structure of HA/Mg–Al LDH nanocomposite can offer more accessible adsorption sites. For ARS, however, the

excessively low adsorption capacity of HA nanoparticles and the mobility of ARS molecules through LDH layers have made Mg–Al LDH a more reliable adsorbent than HA and even HA/Mg–Al LDH nanocomposite.

The proposed mechanisms for dye removal by HA and Mg–Al LDH are also influenced by pH, with HA nanoparticles exhibiting a more pronounced difference between the lowest and highest adsorption capacities. As the electrostatic attraction is directly related to the surface charges and thus the pH, it can be concluded that the electrostatic attraction plays a more significant role in the adsorption of dye on HA, compared to Mg–Al LDH nanoparticles. Furthermore, the effect of pH is similar for all dyes, showing a similar effect on dye removal irrespective of the number of their SO_3^- functional groups. Despite the difference in the number of SO_3^- groups in dye structures, the density of SO_3^- group (the number of groups divided by the molar mass) is almost the same for the dyes used. This similarity in the density of functional groups may be the reason for the similar trend in dye adsorption as a function of pH. The mechanisms for the anionic dyes on HA/Mg–Al LDH have been summarized and proposed in Fig. 11.

Regeneration studies

Figure 12 depicts the results of regeneration studies for HA, Mg–Al LDH, and HA/Mg–Al LDH in adsorbing anionic dyes, presenting the adsorption capacity after the 1st and 5th cycles. The findings indicate that all nanoadsorbents exhibit the potential for effective utilization after five consecutive cycles. The variations in the loss of adsorption capacity, attributed to regeneration cycles, range between 6.23 (minimum reduction for CR adsorption with HA) and 21.16% (maximum reduction for ARS with HA/Mg–Al LDH). The recorded average losses in adsorption capacities for the second, third, fourth, and fifth cycles were 4.02%, 7.60%, 11.02%, and 13.05%, respectively. This pattern suggests a more pronounced loss of adsorption capacity in the second cycle, likely attributed to the irreversible adhesion of dye molecules to specific adsorption sites. This irreversible adhesion is less significant in the next cycles as some sites become preoccupied with dye molecules, resulting in lower adsorption losses during two consecutive regeneration cycles, although the overall adsorption loss is still growing at a slower pace. Notably, the loss of adsorption capacity from the first cycle to the fifth one for all three nanoadsorbents is more when adsorbing ARS.

Comparison with other adsorbents

In order to investigate the highest dye removal capacity of the nanocomposites, three additional experiments were carried out at the optimum condition for each nanocomposite (the optimum pH was maintained at 5, a dosage of 0.2 g/L of adsorbent was used, the adsorption process lasted for 300 min, the experiments

Table 6 Maximum adsorption capacity of different adsorbents toward ARS, CR, and RR120 anionic dyes

| Adsorbent | Dye | Adsorption capacity (mg/g) | Reference |
|--|-------|----------------------------|-------------------------------|
| Multiwalled carbon nanotubes | ARS | 166.6 | (Ghaedi et al. 2011) |
| Au-NPs-AC | ARS | 123.1 | (Roosta et al. 2014) |
| TiO ₂ -NPs coated with CTAB | ARS | 144.9 | (Zolgharnein et al. 2014) |
| Ag-NPs-AC | ARS | 232.6 | (Jamshidi et al. 2015) |
| CS-IMBTESPEDA-SBA-15 | ARS | 50.2 | (Poorebrahim et al. 2016) |
| UiO-66 | ARS | 400.0 | (Embaby et al. 2018) |
| NiFe ₂ O ₄ /PANI composite | ARS | 225.0 | (Liang et al. 2018) |
| PEI@MCNTs | ARS | 196.1 | (Zhang et al. 2019) |
| <i>Schima wallichii</i> biomass | ARS | 91.7 | (Bhomick et al. 2020) |
| Fe ₃ O ₄ @NiO | ARS | 223.3 | (Nodehi et al. 2022) |
| Brookite TiO ₂ | ARS | 140 | (Hmoudah et al. 2022) |
| Fe ₃ O ₄ @Talc | ARS | 11.8 | (Nayl et al. 2022) |
| HA/Mg–Al LDH | ARS | 237.3 | This work |
| Mg-Fe-CO ₃ LDH | CR | 104.1 | (Ahmed and Gasser 2012) |
| Chitosan | CR | 320.0 | (Zúñiga-Zamora et al. 2016) |
| Magnetic hydroxyapatite nanopowder | CR | 402.0 | (Zhang et al. 2016) |
| Fe ₃ O ₄ @MgAl-LDH | CR | 404.6 | (Wu et al. 2017) |
| Hydroxyapatite nanorods | CR | 362.3 | (Guan et al. 2018) |
| Zein-nanohydroxyapatite (Zein/nHAp) | CR | 416.7 | (Ghanavati Nasab et al. 2018) |
| BT-PPH | CR | 138.9 | (Dai et al. 2020) |
| AC | CR | 234 | (Ma et al. 2020) |
| Fe ₃ O ₄ @MIL-53(Al) | CR | 234.4 | (Zhang et al. 2021) |
| Carbon from leaves and stem of water hyacinth | CR | 14.4 | (Extross et al. 2023) |
| Amine-functionalized lignins | CR | 293.3 | (Heo et al. 2022) |
| MIL-88A (Fe) | CR | 607.7 | (Zhao et al. 2023) |
| ZnAl-MHA | CR | 178.6 | (Ahmad et al. 2023) |
| HA/Mg–Al LDH | CR | 423.5 | This work |
| Fe ₃ O ₄ nanoparticles | RR120 | 166.6 | (Absalan et al. 2011) |
| Spirulina platensis microalgae | RR120 | 482.2 | (Cardoso et al. 2012) |
| Modified <i>Jatropha curcas</i> | RR120 | 65.6 | (Prola et al. 2013) |
| Chi-EGDE biofilm | RR120 | 165.3 | (Jawad et al. 2019) |
| <i>Moringa oleifera</i> seed | RR120 | 412.3 | (Çelekli et al. 2019) |
| Quaternary amine modified orange peel powder | RR120 | 344.8 | (Munagapati et al. 2019) |
| Chitosan-epichlorohydrin/zeolite (CHS-ECH/ZL) | RR120 | 284.2 | (Jawad et al. 2020) |
| Bismuth oxychloride/biochar (BiOCl/BC) | RR120 | 116.4 | (Luo et al. 2022) |
| Crosslinked chitosan/coal fly ash composite | RR120 | 237.7 | (Mohammed et al. 2022) |
| NiFe LDH/AC | RR120 | 118.2 | (Munonde et al. 2022) |
| PGMA/mCHT | RR120 | 241 | (Babacan et al. 2022) |
| <i>Ulva prolifera</i> -derived biochar | RR120 | 107.1 | (Mahendran et al. 2021) |
| HA/Mg–Al LDH | RR120 | 429.7 | This work |

were conducted at a temperature of 50 °C, and the initial dye concentration was set at 500 ppm) and the average values, with less than 10% variation, were compared with the results reported in the literature. The results showed that the synthesized nanocomposite in the present study has a rather comparable adsorption capacity with most of the reported adsorbent materials for selected dyes, which makes it a strong candidate for the removal of dye contaminated wastewater (Table 6).

Conclusions

In summary, a nanocomposite of HA/Mg–Al LDH was successfully fabricated through a facile route and was used for the adsorption of three different anionic dyes that are heavily used in the textile industry having different number of SO₃[−] groups. A series of characterization tests proved the proper crystallinity formation of all three as-prepared samples of HA, Mg–Al

LDH, and HA/Mg–Al LDH as well as maintaining both the nanorod structure of HA nanoparticles and hexagonal structure of Mg–Al LDH nanoparticles in the HA/Mg–Al LDH nanocomposite. The higher BET surface area of the new HA/Mg–Al LDH nanocomposite ($111.19 \text{ m}^2/\text{g}$) increased by about 18.8% and 5.9% compared to HA and Mg–Al LDH, which could provide its superior adsorption performance. Under optimized conditions, the nanocomposite demonstrated maximum adsorption capacities of 237.3, 423.5, and 429.7 mg/g for ARS, CR, and RR120, respectively. Significantly, the nanocomposite exhibited a higher dye removal capacity toward anionic dyes with more SO_3^- groups, while Mg–Al LDH was more efficient for ARS removal with only one SO_3^- . In addition, the particle size of the adsorbents was lower than 100 nm, confirming their nanoscale formation. Accordingly, the superior performance of the fabricated nanocomposite in the adsorption of medium and high molecular weight anionic dyes can be attributed to the smaller particle size and higher BET surface area. The effect of several operating variables was investigated on the adsorption efficiency and capacity of the nanocomposite to find optimum conditions. Considering the impact of pH on the adsorption of dyes with different number of SO_3^- functional groups, two different adsorption mechanisms for HA and Mg/Al LDH were proposed. The higher adsorption capacity of HA/Mg–Al LDH nanocomposite was further justified by the proposed mechanisms. Finally, regeneration tests substantiated the potential for consecutive use of the nano-adsorbents, with a modest average adsorption capacity loss of 13% observed in the fifth cycle. This comprehensive investigation provides profound insights into the distinct adsorption behavior and efficiency of synthesized nanocomposites concerning the number of SO_3^- groups present in ARS, CR, and RR120 dyes.

Supplementary Information The online version contains supplementary material available at <https://doi.org/10.1007/s11356-024-32192-6>.

Author contribution Maliheh Heravi: conceptualization, methodology, investigation, and writing the manuscript (original draft, review, and editing).

Varsha Srivastava: conceptualization, conducting characterizing tests utilizing TEM, SEM, and zeta potential analysis.

Ali Ahmadpour: conceptualization, methodology, writing (review and editing), supervision, and funding acquisition.

Vahid Zeynali: conceptualization, methodology, review and editing.

Mika Sillanpää: conceptualization, methodology, writing (review and editing), and funding acquisition.

Funding The authors appreciate the support of both Ferdowsi University of Mashhad and Lappeenranta University of Technology for this work.

Data Availability The data would be provided upon request.

Declarations

Ethical approval This study, titled “Synthesis and Characterization of Hydroxyapatite/Mg–Al LDH for Adsorption of Three Different Anionic Dyes: A Comparative Study of the Effect of the Number of

SO_3^- Groups on Reaction Kinetic, Thermodynamic, and Adsorption Mechanism” conducted by Heravi et al. from Ferdowsi University of Mashhad, has received ethical approval from the appropriate ethics committee. The study adheres to the ethical guidelines and principles and follows the relevant regulations and guidelines for research involving human participants. Informed consent was obtained from all participants involved in the study. The participants were informed about the purpose of the research, the procedures involved, potential risks, and their rights. The data analysis and reporting of findings are conducted with integrity and transparency. The results presented in this study accurately reflect the collected data, and any limitations or biases are acknowledged. This ethical approval statement is provided to assure the Journal of Environmental Science and Pollution Research and its readers that the research has been conducted by ethical standards and guidelines.

Consent to participate Informed consent was obtained from all individual participants included in the study.

Consent for publication The participants have consented to the submission of the case report to the journal.

Competing interests The authors declare no competing interests.

References

- Absalan G, Asadi M, Kamran S et al (2011) Removal of reactive red-120 and 4-(2-pyridylazo) resorcinol from aqueous samples by Fe_3O_4 magnetic nanoparticles using ionic liquid as modifier. *J Hazard Mater* 192:476–484. <https://doi.org/10.1016/j.jhazmat.2011.05.046>
- Ahmad N, Suryani Arsyad F, Royani I et al (2023) High regeneration of ZnAl/NiAl-magnetite humic acid for adsorption of Congo red from aqueous solution. *Inorg Chem Commun* 150. <https://doi.org/10.1016/j.inoche.2023.110517>
- Ahmed IM, Gasser MS (2012) Adsorption study of anionic reactive dye from aqueous solution to Mg-Fe- CO_3 layered double hydroxide (LDH). *Appl Surf Sci* 259:650–656. <https://doi.org/10.1016/j.apsusc.2012.07.092>
- Ai L, Zhang C, Meng L (2011) Adsorption of methyl orange from aqueous solution on hydrothermal synthesized Mg–Al layered double hydroxide. *J Chem Eng Data* 56:4217–4225
- Ayati A, Ahmadpour A, Bamoharram FF et al (2014) Novel Au NPs / Preyssler acid / TiO_2 nanocomposite for the photocatalytic removal of azo dye. *Sep Purif Technol* 133:415–420. <https://doi.org/10.1016/j.seppur.2014.06.055>
- Babacan T, Doğan D, Erdem Ü, Metin AÜ (2022) Magnetically responsive chitosan-based nanoparticles for remediation of anionic dyes: adsorption and magnetically triggered desorption. *Mater Chem Phys* 284. <https://doi.org/10.1016/j.matchemphys.2022.126032>
- Bhomick PC, Supong A, Baruah M et al (2020) Alizarin Red S adsorption onto biomass-based activated carbon: optimization of adsorption process parameters using Taguchi experimental design. *Int J Environ Sci Technol* 17:1137–1148. <https://doi.org/10.1007/s13762-019-02389-1>
- Boujaady E, El Boujaady H, Mourabet M et al (2016) Adsorption of a textile dye on synthesized calcium deficient hydroxyapatite (CDHAp): kinetic and thermodynamic studies. *J Mater Environ Sci* 7:4049–4063
- Cardoso NF, Lima EC, Royer B et al (2012) Comparison of *Spirulina platensis* microalgae and commercial activated carbon as adsorbents for the removal of reactive red 120 dye from aqueous

- effluents. *J Hazard Mater* 241–242:146–153. <https://doi.org/10.1016/j.jhazmat.2012.09.026>
- Çelekli A, Al-nuaimi AI, Bozkurt H (2019) Adsorption kinetic and isotherms of reactive red 120 on *Moringa oleifera* seed as an eco-friendly process. *J Mol Struct* 1195:168–178. <https://doi.org/10.1016/j.molstruc.2019.05.106>
- Cotoruelo LM, Marqués MD, Díaz FJ et al (2010) Equilibrium and kinetic study of Congo red adsorption onto lignin-based activated carbons. *Transp Porous Media* 83:573–590. <https://doi.org/10.1007/s11242-009-9460-8>
- Dai H, Huang Y, Zhang H et al (2020) Direct fabrication of hierarchically processed pineapple peel hydrogels for efficient Congo red adsorption. *Carbohydr Polym* 230. <https://doi.org/10.1016/j.carbpol.2019.115599>
- Daphedar AB, Kakkalamelai S, Faniband B et al (2022) Decolorization of various dyes by microorganisms and green-synthesized nanoparticles: current and future perspective. *Environ Sci Pollut Res*
- Daud M, Hai A, Banat F et al (2019) A review on the recent advances, challenges and future aspect of layered double hydroxides (LDH)–containing hybrids as promising adsorbents for dyes removal. *J Mol Liq* 288:110989. <https://doi.org/10.1016/j.molliq.2019.110989>
- Dotto J, Fagundes-Klen MR, Veit MT et al (2019) Performance of different coagulants in the coagulation/flocculation process of textile wastewater. *J Clean Prod* 208:656–665. <https://doi.org/10.1016/j.jclepro.2018.10.112>
- Embaby MS, Elwany SD, Setyaningsih W, Saber MR (2018) The adsorptive properties of UiO-66 towards organic dyes: a record adsorption capacity for the anionic dye Alizarin Red S. *Chin J Chem Eng* 26:731–739. <https://doi.org/10.1016/j.cjche.2017.07.014>
- Errais E, Duplay J, Elhabiri M et al (2012) Anionic RR120 dye adsorption onto raw clay: surface properties and adsorption mechanism. *Colloids Surf A Physicochem Eng Asp* 403:69–78. <https://doi.org/10.1016/j.colsurfa.2012.03.057>
- Extross A, Waknis A, Tagad C et al (2023) Adsorption of congo red using carbon from leaves and stem of water hyacinth: equilibrium, kinetics, thermodynamic studies. *Int J Environ Sci Technol* 20:1607–1644. <https://doi.org/10.1007/s13762-022-03938-x>
- Fayyazbakhsh F, Solati-hashjin M, Keshtkar A, Ali M (2017) Novel layered double hydroxides-hydroxyapatite / gelatin bone tissue engineering scaffolds : fabrication, characterization, and in vivo study. *Mater Sci Eng C* 76:701–714. <https://doi.org/10.1016/j.msec.2017.02.172>
- Fried R, Oprea I, Fleck K, Rudroff F (2022) Biogenic colourants in the textile industry – a promising and sustainable alternative to synthetic dyes. *Green Chem* 24:13–35. <https://doi.org/10.1039/d1gc02968a>
- Ghaedi M, Hassanzadeh A, Kokhdan SN (2011) Multiwalled carbon nanotubes as adsorbents for the kinetic and equilibrium study of the removal of alizarin red S and morin. *J Chem Eng Data* 56:2511–2520
- Ghaedi M, Najibi A, Hossainian H et al (2012) Kinetic and equilibrium study of alizarin red S removal by activated carbon. *Toxicol Environ Chem* 94:40–48
- Ghanavati Nasab S, Semnani A, Teimouri A et al (2018) Removal of Congo red from aqueous solution by hydroxyapatite nanoparticles loaded on zein as an efficient and green adsorbent: response surface methodology and artificial neural network-genetic algorithm. *J Polym Environ* 26:3677–3697. <https://doi.org/10.1007/s10924-018-1246-z>
- Googerdchian F, Moheb A, Emadi R, Asgari M (2018) Optimization of Pb (II) ions adsorption on nanohydroxyapatite adsorbents by applying Taguchi method. *J Hazard Mater* 349:186–194. <https://doi.org/10.1016/j.jhazmat.2018.01.056>
- Guan Y, Cao W, Wang X, Marchetti A (2018) Hydroxyapatite nanorods for the fast removal of congo red dye from aqueous solution. *Mater Res Express* 5:065053
- Gusain D, Bux F, Chandra Y (2014) Abatement of chromium by adsorption on nanocrystalline zirconia using response surface methodology. *J Mol Liq* 197:131–141. <https://doi.org/10.1016/j.molliq.2014.04.026>
- Hameed BB, Ismail ZZ (2020) New application of Orchis mascula as a biocarrier for immobilization of mixed cells for biodegradation and detoxification of reactive azo dyes. *Environ Sci Pollut Res* 27:38732–38744. <https://doi.org/10.1007/s11356-020-09984-7>
- Harja M, Ciobanu G (2018) Studies on adsorption of oxytetracycline from aqueous solutions onto hydroxyapatite. *Sci Total Environ* 628–629:36–43. <https://doi.org/10.1016/j.scitotenv.2018.02.027>
- Haro NK, Del Vecchio P, Marcilio NR, Fêris LA (2017) Removal of atenolol by adsorption – study of kinetics and equilibrium. *J Clean Prod* 154:214–219. <https://doi.org/10.1016/j.jclepro.2017.03.217>
- Heo JW, An L, Chen J et al (2022) Preparation of amine-functionalized lignins for the selective adsorption of methylene blue and Congo red. *Chemosphere* 295. <https://doi.org/10.1016/j.chemosphere.2022.133815>
- Hmoudah M, El-Qanni A, Abuhatab S et al (2022) Competitive adsorption of alizarin red S and bromocresol green from aqueous solutions using brookite TiO₂ nanoparticles: experimental and molecular dynamics simulation. *Environ Sci Pollut Res* 29:77992–78008. <https://doi.org/10.1007/s11356-022-21368-7>
- Hosseini S, Khan MA, Malekbala MR et al (2011) Carbon coated monolith, a mesoporous material for the removal of methyl orange from aqueous phase: adsorption and desorption studies. *Chem Eng J* 171:1124–1131. <https://doi.org/10.1016/j.cej.2011.05.010>
- Huang R (2017) Adsorption of methyl orange onto protonated cross-linked chitosan. *Arab J Chem* 10:24–32. <https://doi.org/10.1016/j.arabjc.2013.05.017>
- Huang M, Zhang Y, Xiang W et al (2019) Efficient adsorption of Mn(II) by layered double hydroxides intercalated with diethylenetriaminepentaacetic acid and the mechanistic study. *J Environ Sci* 85:56–65. <https://doi.org/10.1016/j.jes.2019.04.011>
- Iftekhhar S, Srivastava V, Ben S, Sillanpää M (2018) Fabrication of novel metal ion imprinted xanthan gum-layered double hydroxide nanocomposite for adsorption of rare earth elements. *Carbohydr Polym* 194:274–284. <https://doi.org/10.1016/j.carbpol.2018.04.054>
- Iftekhhar S, Srivastava V, Ramasamy DL et al (2018) A novel approach for synthesis of exfoliated biopolymeric-LDH hybrid nanocomposites via in-situ coprecipitation with gum Arabic: application towards REEs recovery. *Chem Eng J* 347:398–406. <https://doi.org/10.1016/j.cej.2018.04.126>
- Inglezakis VJ, Zorpas AA (2019) Heat of adsorption, adsorption energy and activation energy in adsorption and ion exchange systems. *Desalin Water Treat* 39:149–157. <https://doi.org/10.5004/dwt.2012.3000>
- Islam T, Repon MR, Islam T et al (2023) Impact of textile dyes on health and ecosystem: a review of structure, causes, and potential solutions. *Environ Sci Pollut Res* 30:9207–9242
- Jamshidi M, Ghaedi M, Dashtian K et al (2015) Ultrasound-assisted removal of Al³⁺ ions and alizarin red S by activated carbon engrafted with Ag nanoparticles: central composite design and genetic algorithm optimization. *RSC Adv* 5:59522–59532. <https://doi.org/10.1039/c5ra10981g>
- Jawad AH, Abdulhameed AS, Reghioa A, Yaseen ZM (2020) Zwitterion composite chitosan-epichlorohydrin/zeolite for adsorption of methylene blue and reactive red 120 dyes. *Int J Biol Macromol* 163:756–765. <https://doi.org/10.1016/j.ijbiomac.2020.07.014>
- Jawad AH, Mamat NFH, Hameed BH, Ismail K (2019) Biofilm of cross-linked chitosan-ethylene glycol diglycidyl ether for removal of reactive red 120 and methyl orange: adsorption and mechanism studies. *J Environ Chem Eng* 7. <https://doi.org/10.1016/j.jece.2019.102965>
- Jiang DB, Jing C, Yuan Y et al (2019) 2D–2D growth of NiFe LDH nanoflakes on montmorillonite for cationic and anionic dye

- adsorption performance. *J Colloid Interface Sci.* <https://doi.org/10.1016/j.jcis.2019.01.022>
- Klinkaewnarong J, Swatsitang E, Maensiri S (2009) Nanocrystalline hydroxyapatite powders by a chitosan–polymer complex solution route : synthesis and characterization. *Solid State Sci* 11:1023–1027. <https://doi.org/10.1016/j.solidstatesciences.2009.02.003>
- Li M, Chen M, Lee SLJ, Lin S (2023) Facile fabrication of a 2D/2D CoFe-LDH/g-C₃N₄ nanocomposite with enhanced photocatalytic tetracycline degradation. *Environ Sci Pollut Res* 30:4709–4720. <https://doi.org/10.1007/s11356-022-22554-3>
- Liang Y, He Y, Zhang Y (2018) Adsorption property of alizarin red S by NiFe₂O₄/polyaniline magnetic composite. *J Environ Chem Eng* 6:416–425. <https://doi.org/10.1016/j.jece.2017.12.022>
- Luo Y, Wang Y, Zhu Y et al (2022) Ball-milled bismuth oxychloride/biochar nanocomposites with rich oxygen vacancies for reactive red-120 adsorption in aqueous solution. *Biochar* 4. <https://doi.org/10.1007/s42773-022-00147-0>
- Ma YZ, Zheng DF, Mo ZY et al (2018) Magnetic lignin-based carbon nanoparticles and the adsorption for removal of methyl orange. *Colloids Surf A Physicochem Eng Asp* 559:226–234. <https://doi.org/10.1016/j.colsurfa.2018.09.054>
- Ma M, Ying H, Cao F et al (2020) Adsorption of congo red on mesoporous activated carbon prepared by CO₂ physical activation. *Chinese J Chem Eng* 28:1069–1076. <https://doi.org/10.1016/j.cjche.2020.01.016>
- Mahendran S, Gokulan & R, Aravindan & A, et al (2021) Production of Ulva prolifera derived biochar and evaluation of adsorptive removal of reactive red 120: batch, isotherm, kinetic, thermodynamic and regeneration studies. <https://doi.org/10.1007/s13399-021-01483-0/Published>
- Mahmoodi V, Ahmadpour A, Bastami TR, Mosavian MTH (2018) PVP assisted synthesis of high efficient BiOI/graphene oxide nanohybrid and its photocatalytic performance in degradation of organic dye pollutants. *Sol Energy* 176:483–495. <https://doi.org/10.1016/j.solener.2018.10.056>
- Mallakpour S, Hatami M (2019) An effective, low-cost and recyclable bio-adsorbent having amino acid intercalated LDH@Fe₃O₄/PVA magnetic nanocomposites for removal of methyl orange from aqueous solution. *Appl Clay Sci* 174:127–137. <https://doi.org/10.1016/j.clay.2019.03.026>
- Marincaş L, Turdean GL, Toşa M, et al (2021) Hydroxyapatite and silicon-modified hydroxyapatite as drug carriers for 4-aminopyridine. *Crystals* 11. <https://doi.org/10.3390/cryst11091124>
- Mohammed IA, Malek NNA, Jawad AH et al (2022) Box-Behnken design for optimizing synthesis and adsorption conditions of covalently crosslinked chitosan/coal fly ash composite for reactive red 120 dye removal. *J Polym Environ* 30:3447–3462. <https://doi.org/10.1007/s10924-022-02443-z>
- Mudhoo A, Mohan D, Pittman CU et al (2021) Adsorbents for real-scale water remediation: gaps and the road forward. *J Environ Chem Eng* 9. <https://doi.org/10.1016/j.jece.2021.105380>
- Munagapati VS, Wen J-C, Pan C-L et al (2019) Enhanced adsorption performance of reactive red 120 azo dye from aqueous solution using quaternary amine modified orange peel powder. *J Mol Liq* 285:375–385. <https://doi.org/10.1016/j.molliq.2019.04.081>
- Munonde TS, September NP, Mpupa A, Nomngongo PN (2022) Two agitation routes for the adsorption of reactive red 120 dye on NiFe LDH/AC nanosheets from wastewater and river water. *Appl Clay Sci* 219. <https://doi.org/10.1016/j.clay.2022.106438>
- Muráth S, Somosi Z, Tóth IY et al (2017) Delaminating and restacking MgAl-layered double hydroxide monitored and characterized by a range of instrumental methods. *J Mol Struct* 1140:77–82. <https://doi.org/10.1016/j.molstruc.2016.10.056>
- Naseem S, Gevers BR, Labuschagné FJWJ, Leuteritz A (2020) Preparation of photoactive transition-metal layered double hydroxides (LDH) to replace dye-sensitized materials in solar cells. *Materials (basel)* 13:1–12. <https://doi.org/10.3390/ma13194384>
- Nayl AA, Abd-Elhamid AI, Ahmed IM, Bräse S (2022) Preparation and characterization of magnetite Talc (Fe₃O₄@Talc) nanocomposite as an effective adsorbent for Cr(VI) and alizarin red S dye. *Materials (Basel)* 15. <https://doi.org/10.3390/ma15093401>
- Nodehi R, Shayesteh H, Rahbar-Kelishami A (2022) Fe₃O₄@NiO core-shell magnetic nanoparticle for highly efficient removal of alizarin red S anionic dye. *Int J Environ Sci Technol* 19:2899–2912. <https://doi.org/10.1007/s13762-021-03399-8>
- Omrani E, Ahmadpour A, Heravi M, Bastami TR (2022) Novel ZnTi LDH/h-BN nanocomposites for removal of two different organic contaminants: simultaneous visible light photodegradation of Amaranth and Diazepam. *J Water Process Eng* 47. <https://doi.org/10.1016/j.jwpe.2022.102581>
- Pai S, M Kini S, Selvaraj R, Pugazhendhi A (2020) A review on the synthesis of hydroxyapatite, its composites and adsorptive removal of pollutants from wastewater. *J Water Process Eng* 38. <https://doi.org/10.1016/j.jwpe.2020.101574>
- Pereira Rocha RL, Silva TL, Araujo FP et al (2021) Gallium-containing hydroxyapatite as a promising material for photocatalytic performance. *Minerals* 11. <https://doi.org/10.3390/min11121347>
- Piri F, Mollahosseini A, Khadir A, Milani Hosseini M (2019) Enhanced adsorption of dyes on microwave-assisted synthesized magnetic zeolite-hydroxyapatite nanocomposite. *J Environ Chem Eng* 7:103338. <https://doi.org/10.1016/j.jece.2019.103338>
- Poorebrahim F, Ghaedi M, Dashtian K et al (2016) Simultaneous removing of Pb²⁺ ions and alizarin red S dye after their complexation by ultrasonic waves coupled adsorption process: spectrophotometry detection and optimization study. *Ultrason-Sonochemistry*. <https://doi.org/10.1016/j.ultsonch.2016.09.002>
- Prola LDT, Acayanka E, Lima EC et al (2013) Comparison of Jatropha curcas shells in natural form and treated by non-thermal plasma as biosorbents for removal of Reactive Red 120 textile dye from aqueous solution. *Ind Crop Prod* 46:328–340. <https://doi.org/10.1016/j.indcrop.2013.02.018>
- Rapo E, Tonk S (2021) Factors affecting synthetic dye adsorption; desorption studies : a review of results from the last five years. *Molecules* 26:5419–5450
- Roosta M, Ghaedi M, Mohammadi M (2014) Removal of alizarin red S by gold nanoparticles loaded on activated carbon combined with ultrasound device : optimization by experimental design methodology. *Powder Technol* 267:134–144. <https://doi.org/10.1016/j.powtec.2014.06.052>
- Sadeghizadeh A, Ebrahimi F, Heydari M et al (2019) Adsorptive removal of Pb (II) by means of hydroxyapatite/chitosan nanocomposite hybrid nano-adsorbent: ANFIS modeling and experimental study. *J Environ Manage* 232:342–353. <https://doi.org/10.1016/j.jenvman.2018.11.047>
- Saha P, Chowdhury S (2011) Insight into adsorption thermodynamics. *Thermodynamics* 349–364
- Saharan P, Kumar V, Kaushal I et al (2023) A comprehensive review on the metal-based green valorized nanocomposite for the remediation of emerging colored organic waste. *Environ Sci Pollut Res* 30:45677–45700. <https://doi.org/10.1007/s11356-023-25998-3>
- Shakir M, Zia I, Rehman A, Ullah R (2018) Fabrication and characterization of nanoengineered biocompatible n-HA/chitosan-tamarind seed polysaccharide: bio-inspired nanocomposites for bone tissue engineering. *Int J Biol Macromol* 111:903–916. <https://doi.org/10.1016/j.ijbiomac.2018.01.035>
- Sheng G, Tang Y, Linghu W et al (2016) Enhanced immobilization of ReO₄⁻ by nanoscale zerovalent iron supported on layered double hydroxide via an advanced XAFS approach : Implications for TCO₄⁻ sequestration. *Appl Catal B Environ* 192:268–276. <https://doi.org/10.1016/j.apcatb.2016.04.001>

- Srivastava V, Sharma YC, Sillanpää M (2015) Application of response surface methodology for optimization of Co (II) removal from synthetic wastewater by adsorption on NiO nanoparticles. *J Mol Liq* 211:613–620. <https://doi.org/10.1016/j.molliq.2015.07.056>
- Srivastava V, Iftikhar S, Wang Z et al (2018) Synthesis and application of biocompatible nontoxic nanoparticles for reclamation of Ce^{3+} from synthetic wastewater : toxicity assessment, kinetic, isotherm and thermodynamic study. *J Rare Earths* 36:994–1006. <https://doi.org/10.1016/j.jre.2018.03.005>
- Tanhaei B, Ayati A, Lahtinen M, Sillanpää M (2015) Preparation and characterization of a novel chitosan/Al₂O₃/magnetite nanoparticles composite adsorbent for kinetic, thermodynamic and isotherm studies of Methyl Orange adsorption. *Chem Eng J* 259:1–10. <https://doi.org/10.1016/j.cej.2014.07.109>
- Tanhaei B, Ayati A, Lahtinen M et al (2016) A magnetic mesoporous chitosan based core-shells biopolymer for anionic dye adsorption : kinetic and isothermal study and application of ANN. *J Appl Polym Sci* 43466:1–11. <https://doi.org/10.1002/app.43466>
- Wu C, Scott J, Shea JE (2012) Binding of Congo red to amyloid protofibrils of the alzheimer A β 9-40 peptide probed by molecular dynamics simulations. *Biophys J* 103:550–557. <https://doi.org/10.1016/j.bpj.2012.07.008>
- Wu X, Li B, Wen X (2017) Synthesis and adsorption properties of hierarchical Fe₃O₄@MgAl-LDH magnetic microspheres. *J Nanoparticle Res* 131. <https://doi.org/10.1007/s11051-017-3803-0>
- Xiong T, Yuan X, Wang H et al (2019) Highly efficient removal of diclofenac sodium from medical wastewater by Mg/Al layered double hydroxide-poly (m-phenylenediamine) composite. *Chem Eng J* 366:83–91. <https://doi.org/10.1016/j.cej.2019.02.069>
- Zeynali V, Mousavi SM, Saljoughi E et al (2023) Chitosan/polyvinyl alcohol/hydroxyapatite nanocomposite membrane for the efficient adsorption of Congo red anionic dye. *Polym Compos* 44:4227–4242. <https://doi.org/10.1002/pc.27393>
- Zhang F, Ma B, Jiang X, Ji Y (2016) Dual function magnetic hydroxyapatite nanopowder for removal of malachite green and Congo red from aqueous solution. *Powder Technol* 302:207–214. <https://doi.org/10.1016/j.powtec.2016.08.044>
- Zhang Z, Gora-Marek K, Watson JS et al (2019) Recovering waste plastics using shape-selective nano-scale reactors as catalysts. *Nat Sustain* 2:39–42. <https://doi.org/10.1038/s41893-018-0195-9>
- Zhang G, Wo R, Sun Z, et al (2021) Effective magnetic mofs adsorbent for the removal of bisphenol a, tetracycline, Congo red and methylene blue pollutions. *Nanomaterials* 11. <https://doi.org/10.3390/nano11081917>
- Zhao S, Li Y, Wang M et al (2023) Efficient adsorption of Congo red by micro/nano MIL-88A (Fe, Al, Fe-Al)/chitosan composite sponge: preparation, characterization, and adsorption mechanism. *Int J Biol Macromol* 239. <https://doi.org/10.1016/j.ijbiomac.2023.124157>
- Zolgharnein J, Bagtash M, Asanjarani N (2014) Hybrid central composite design approach for simultaneous optimization of removal of alizarin red S and indigo carmine dyes using Cetyltrimethylammonium bromide-modified TiO₂ nano-particles. Elsevier
- Zúñiga-Zamora A, García-Mena J, Cervantes-González E (2016) Removal of Congo red from the aqueous phase by chitin and chitosan from waste shrimp. *Desalin Water Treat* 57:14674–14685. <https://doi.org/10.1080/19443994.2015.1065444>

Publisher's Note Springer Nature remains neutral with regard to jurisdictional claims in published maps and institutional affiliations.

Springer Nature or its licensor (e.g. a society or other partner) holds exclusive rights to this article under a publishing agreement with the author(s) or other rightsholder(s); author self-archiving of the accepted manuscript version of this article is solely governed by the terms of such publishing agreement and applicable law.